Progress Report
July 1, 1996 - December 30, 1996

NASA-UVA LIGHT AEROSPACE ALLOY AND STRUCTURES TECHNOLOGY PROGRAM (LA^2ST)

Supplement: RESEARCH ON MATERIALS FOR THE HIGH SPEED CIVIL TRANSPORT

NASA-LaRC Grant NAG-1-745

Submitted to:

National Aeronautics and Space Administration
Langley Research Center
Hampton, VA 23681-0001

Attention: Mr. Joseph S. Murray, Grants Officer, MS 126

For Review by:

Mr. Dennis L. Dicus, Grants Monitor
Metallic Materials Branch, MS 188A

Submitted by:

Richard P. Gangloff
Professor

and

Edgar A. Starke, Jr.
University Professor

SEAS Report No. UVA/528266/MSE97/122
March 1997

DEPARTMENT OF MATERIALS SCIENCE AND ENGINEERING

SCHOOL OF
ENGINEERING & APPLIED SCIENCE

University of Virginia
Thornton Hall
Charlottesville, VA 22903

UNIVERSITY OF VIRGINIA
School of Engineering and Applied Science

The University of Virginia's School of Engineering and Applied Science has an undergraduate enrollment of approximately 1,500 students with a graduate enrollment of approximately 600. There are 160 faculty members, a majority of whom conduct research in addition to teaching.

Research is a vital part of the educational program and interests parallel academic specialties. These range from the classical engineering disciplines of Chemical, Civil, Electrical, and Mechanical and Aerospace to newer, more specialized fields of Applied Mechanics, Biomedical Engineering, Systems Engineering, Materials Science, Nuclear Engineering and Engineering Physics, Applied Mathematics and Computer Science. Within these disciplines there are well equipped laboratories for conducting highly specialized research. All departments offer the doctorate; Biomedical and Materials Science grant only graduate degrees. In addition, courses in the humanities are offered within the School.

The University of Virginia (which includes approximately 2,000 faculty and a total of full-time student enrollment of about 17,000), also offers professional degrees under the schools of Architecture, Law, Medicine, Nursing, Commerce, Business Administration, and Education. In addition, the College of Arts and Sciences houses departments of Mathematics, Phyics, Chemistry and others relevant to the engineering research program. The School of Engineering and Applied Science is an integral part of this University community which provides opportunities for interdisciplinary work in pursuit of the basic goals of education, research, and public service.

TABLE OF CONTENTS

EXECUTIVE SUMMARY

This report documents the progress achieved over the past 6 to 12 months on four graduate student projects conducted within the NASA-UVa Light Aerospace Alloy and Structures Technology Program. These studies were aimed specifically at light metallic alloy issues relevant to the High Speed Civil Transport. The accomplishments presented in this report are summarized as follows.

Research on Hydrogen-Enhanced Fracture of High-Strength Titanium Alloy Sheet refined successfully the high resolution R-curve method necessary to characterize initiation and growth fracture toughnesses. For solution treated and aged Low Cost Beta without hydrogen precharging, fracture is by ductile transgranular processes at 25°C, but standardized initiation toughnesses are somewhat low and crack extension is resolved at still lower K-levels. This fracture resistance is degraded substantially, by between 700 and 1000 wppm of dissolved hydrogen, and a fracture mode change is affected. The surface oxide on β-titanium alloys hinders hydrogen uptake and complicates the electrochemical introduction of low hydrogen concentrations that are critical to applications of these alloys. Ti-15-3 sheet was obtained for study during the next reporting period. *(Hayes and Gangloff)*

Research on Mechanisms of Deformation and Fracture in High-Strength Titanium Alloys is examining the microstructure and fatigue resistance of very thin sheet. Aging experiments on 0.14 mm thick (0.0055 inch) foil show microstructural agility that may be used to enhance fatigue performance. Fatigue testing of Ti-15-3 sheet has begun. The effects of various thermo-mechanical processing regimens on mechanical properties will be examined and deformation modes identified. *(Kazanjian, Hargarter, and Starke)*

Research on the Effect of Texture and Precipitates on Mechanical Property Anisotropy of Al-Cu-Mg-X and Al-Cu alloys demonstrated that models predict a minor influence of stress-induced alignment of Θ', caused by the application of a tensile stress during aging, on the yield stress anisotropy of both modified AA2519 and a model Al-Cu binary alloy. This project is no longer included in the NASA-UVa LA^{2}ST program. *(Hargarter, and Starke)*

Research on the Creep Behavior and Microstructural stability of Al-Cu-Mg-Ag and Al-Cu-Li-Mg-Ag showed that the creep resistance of three candidate aluminum alloys (C415, C416 and ML377) was much superior compared to that of the current Concorde alloy, AA2618. Creep induced change in precipitates at grain boundaries was observed in the alloy which exhibits the highest creep strain of the three examined. The other two alloys developed no detectable microstructural changes at grain boundaries under the creep conditions tested.
(Kazanjian, Wang and Starke)

INTRODUCTION

Since 1986, the NASA-Langley Research Center has sponsored the NASA-UVa Light Alloy and Structures Technology (LA^2ST) Program at the University of Virginia (UVa). The fundamental objective of the LA^2ST program is to conduct interdisciplinary graduate student research on the performance of next generation, light-weight aerospace alloys, composites and thermal gradient structures. The LA^2ST program has aimed to produce relevant data and basic understanding of material mechanical response, environmental/corrosion behavior, and microstructure; new monolithic and composite alloys; advanced processing methods; measurement and modeling advances; and a pool of educated graduate students for aerospace technologies. The scope of the LA^2ST Program is broad. Research areas include: (1) *Mechanical and Environmental Degradation Mechanisms in Advanced Light Metals and Composites*, (2) *Aerospace Materials Science*, (3) *Mechanics of Materials for Aerospace Structures*, and (4) *Thermal Gradient Structures*. A substantial series of semi-annual progress reports issued since 1987 document the technical objectives, experimental or analytical procedures, and detailed results of graduate student research in these topical areas.

As documented in the most recent progress report,[1] LA^2ST productivity since 1986 includes: 125 publications (83 archival journal or reviewed book publications), 24 PhD dissertations or MS theses, 122 external technical presentations, 20 NASA progress reports and 4 NASA Contractor Reports. Since 1986, 36 graduate students, including 33 citizens of the United States, have been involved with LA^2ST research; 24 have received the MS or PhD degree. Five post-doctoral research associates have participated in LA^2ST research, along with a total of 13 faculty.

In October of 1991, E.A. Starke proposed a substantial supplement to the base LA^2ST Program. The objective of this research was to involve UVa faculty with engineering scientists from aluminum alloy producers and airframe manufacturers in a broad research program to develop light aluminum alloys and composites for elevated temperature-long time High Speed Civil

---

1 R.P. Gangloff and E.A. Starke, Jr., *NASA-UVA Light Aerospace Alloy and Structures Technology Program,* Report No. UVA/528266/MS97/121, University of Virginia, Charlottesville, VA, February, 1997.

Transport (HSCT) applications.[2, 3] NASA-Langley Research Center (LaRC), ALCOA, Allied-Signal, Boeing, McDonnell Douglas, Reynolds Metals and UVa joined in a research effort to identify the most promising aluminum-based materials with respect to major structural use on the HSCT and to further develop those materials. This research began in January of 1992 and results were reported separately from the LA^{2}ST program.[4] In 1994 HSCT research at UVa was expanded to include titanium alloys, and collaborations were implemented with RMI Titanium Company and TIMET. These titanium projects were reported in base LA^{2}ST progress reports, as was aluminum HSCT work performed during 1995 and beyond. In mid-1996 NASA requested that those LA^{2}ST projects dealing with HSCT materials issues be reported separately. This progress report is the first in this regard.

Four HSCT research projects were conducted at UVa in 1996, involving two PhD graduate students, Sean P. Hayes (advised by Professor Gangloff) and Susan M. Kazanjian (advised by Professor Starke), as well as a Post-doctoral Research Associate supervised by E.A. Starke. Research progress, recorded during the period from July 1, 1996 to December 31, 1996, is summarized in the following four sections. Each section contains a problem statement, research objective, approach, recent results, conclusions, and future milestones. These discussions are expanded somewhat since this is the first progress report that is disseminated to those active in HSCT research and development.

---

2 R.P. Gangloff, E.A. Starke, Jr., J.M. Howe and F.E. Wawner, *NASA-UVa Light Aerospace Alloy and Structures Technology Program: Supplement on Aluminum Based Materials for High Speed Aircraft*, Proposal No. MS NASA/LaRC-5215-92, University of Virginia, 1991.

3 R.P. Gangloff, E.A. Starke, Jr., J.M. Howe and F.E. Wawner, *NASA-UVa Light Aerospace Alloy and Structures Technology Program: Supplement on Aluminum Based Materials for High Speed Aircraft*, Proposal No. MSE NASA/LaRC-5691-93, University of Virginia, 1992.

4 E.A. Starke, Jr., *NASA-UVa Light Aerospace Alloy and Structures Technology Program Supplement: Aluminum-Based Materials for High Speed Aircraft*, NASA Contractor Report 4517, June, 1993.

RESEARCH RESULTS

Project 1: Mechanisms of Deformation and Fracture in High-Strength Titanium Alloys: Effect of Dissolved Hydrogen

Sean P. Hayes and Richard P. Gangloff

Background and Problem Statement

Metastable β-titanium alloys are candidates for the airframe of the High Speed Civil Transport (HSCT). Operating temperatures of this Mach 2.0 to 2.4 aircraft are expected to range from cryogenic levels to 200°C, with component life on the order of 60,000 hours. The use of titanium alloys for this application is based on the need to function at the higher levels of this temperature range, while achieving three property goals: high strength, high fracture toughness, and high elastic modulus. This project focuses on materials that meet the high strength goal, with the following target properties for sheet microstructures: σ_{UTS} = 1450 MPa with E = 110 GPa, K_{IC} = 66 MPa$\sqrt{m}$ and $K_{Applied}$ = 110 MPa$\sqrt{m}$. K_{IC} is the standard plane strain fracture toughness, while $K_{Applied}$ is a critical value of the stress intensity required to fracture unstably a relatively large and thin sheet specimen, presumably under dominant plane stress deformation.

Two metastable β-titanium alloys in sheet form are being investigated, including TIMETAL Low Cost Beta (LCB: Ti-6.8Mo-4.5Fe-1.5Al-0.09O, by weight pct) and TIMETAL 15-3 (Ti-15-3; Ti-15V-3Al-3Cr-3Zn-0.13O). Metastable β-titanium alloys contain elements which stabilize the body centered cubic β phase and lower the martensite start temperature below room temperature to prevent martensite formation upon cooling. A high strength microstructure is achieved typically by solution treatment above the β-transus, cooling to room temperature so that an all-β microstructure remains, and aging in the α+β region to produce the desired volume fraction and morphology of the hexagonal close packed α phase in a continuous β matrix. This is the so-called STA condition.

Potential problems and uncertainties are associated with the complex nature of the fracture processes in titanium alloys, and with the possibility of failure modes that depend on time. Issues include the proper selection of alloy composition and thermo-mechanical process, based on understanding of fracture damage mechanisms, as well as the potential for long-term alloy

degradation due to problems such as hydrogen embrittlement.

Ductile Fracture

Ductile fracture is insufficiently characterized and understood in STA β-Ti alloys. In these alloys, microstructure can be varied extensively by alloy composition, forging and rolling history, and final heat treatment.[1] Variations in microstructure (i.e., volume fraction, morphology, and size of both primary α-phase and α-precipitates) result in significant changes in plastic deformation, partitioned uniquely between the two phases, as well as in differences in microvoid nucleation, growth and coalescence behavior. These factors in turn alter fracture resistance.

For example, by altering the thermo-mechanical processing and microstructure of Ti-10V-2Fe-3Al, yield strengths ranging from 900 to 1450 MPa were achieved.[2] Tensile ductility, as well as K_{IC} and K-Δa resistance curves, varied dramatically with yield strength for microstructures developed by α/β solution treatment followed by aging. Crack-growth initiation occurred at a stress intensity of 70 MPa$\sqrt{m}$ for a yield strength of 1072 MPa, but at 24 MPa$\sqrt{m}$ for a yield strength of 1312 MPa.[2] The complex microstructural origins of damage and fracture processes that occur in these alloys hinder understanding of ductile fracture.[1,3-4] Considering the case cited above, a change in ductile fracture mechanism was observed for Ti-10-2-3 when comparing low and high strength microstructures. Intense strain localization was cited as the cause of the exceptionally sharp decline in fracture toughness with increasing yield strength. This localization was traced to stress concentration in the β-phase due to extraordinary high work hardening in α-precipitates sized below a critical level. The small α-precipitates, produced by aging to develop high strength, were responsible for both the slip localization and sharp toughness decrease in the α/β-processed microstructure.

The fracture toughness behavior of β-solution treated microstructures is uncertain. Further, the behavior of sheet microstructures in this strength range is not defined, given the emphasis to date on plate and forgings of STA β-titanium alloys.

Hydrogen Embrittlement

Dissolved hydrogen in β-titanium alloy microstructures may pose a long-term embrittlement threat. The diffusivity of hydrogen is much greater in the body centered cubic β-phase than in the α-phase. This rapid diffusivity, coupled with the high hydrogen solubility of the β-phase, increase the likelihood of hydrogen pick-up during processing of different β alloys compared to α or α+β alloys.[4] Additionally, titanium alloys can pick-up hydrogen during long-

term service, due to either localized corrosion or a corrosion-strain interaction. Hydrogen uptake (and egress-loss) is normally blocked by the surface oxide which is an extremely effective hydrogen barrier. For hydrogen uptake to occur, this film must be destabilized either chemically or mechanically. For example, data from Lockheed-Martin show that the dissolved hydrogen concentration in LCB doubles from 230 to 400 wppm H due to chemical milling. Additionally, the starting hydrogen content of various β-titanium alloys can differ between 30 and 300 wppm.

Although metastable β-titanium alloys are claimed to tolerate dissolved hydrogen[5], substantial results show that plate and bar microstructures of STA alloys are sensitive to severe intergranular and transgranular hydrogen embrittlement when stressed at room temperature. Alloys such as Beta-21S, Ti-15-3, and Beta-C are embrittled at 25°C by predissolved hydrogen produced electrochemically at concentrations well below those required to hydride the β-phase.[6-10] This behavior is demonstrated by circumferentially notched tensile bars, which showed reductions in maximum longitudinal stress and plastic strain, as well as changes in fracture modes with increasing hydrogen concentrations. For example, in the peak aged conditions, high strength STA Beta-21S and Beta-C exhibited abrupt decreases in strength and ductility above approximately 1000 and 1500 wppm H, respectively, while Ti-15-3 exhibited a linear decrease in strength and ductility with increasing hydrogen concentration. Reductions in mechanical properties due to predissolved hydrogen have been correlated with changes in fracture mechanisms as described by Scully, Young and Gaudett.[6-10]

The solution treated (ST) single β -phase condition of these alloys is immune to internal hydrogen embrittlement. One significant difference between the ST and STA conditions is yield strength. However, results from cold worked ST Beta-C, processed to yield strengths comparable to the STA condition but retaining an all β microstructure, indicate that high yield strength alone does not account for the differences in susceptibility to hydrogen embrittlement.[10] Instead, microstructural features, particularly associated with the α-phase, are implicated as essential to cause hydrogen embrittlement in STA β-titanium alloys.

Literature results have shown that hydrogen degrades the fracture resistance of β-titanium alloys[6-10], but studies are incomplete in several important regards. First, detailed fracture mechanics properties have not been measured to characterize hydrogen embrittlement relevant to predicting component design. Second, hydrogen embrittlement studies have focused on specimens from plate and bar stock that was β-solution treated. Microstructural features have been implicated

in contributing to hydrogen embrittlement, but sheet microstructures and α/β heat treatments have not been investigated. Third, there is no information on the hydrogen embrittlement behavior of very high strength STA β-titanium alloys. Fourth, hydrogen embrittlement studies have focused on investigating high hydrogen concentrations (greater than 1000 wppm), while the low hydrogen concentration regime (200 to 1000 wppm) is relatively unexplored. This regime is important to the long term performance of structural components in the HSCT. Finally, the effects of modestly elevated temperatures, as well as cryogenic temperatures, on predissolved-hydrogen embrittlement are unknown since only room temperature experiments have been performed. It is well known that dissolved hydrogen concentration, temperature, yield strength, and loading rate affect, interactively, the extent of internal hydrogen embrittlement in alloy steels. Similar effects are anticipated for β-titanium alloys. Apart from these phenomenological issues, the mechanism for hydrogen embrittlement of high strength β-titanium alloys has not been established.

Objectives

From an engineering perspective, the broad objective of this research is to define the hydrogen concentration and microstructural conditions that promote internal hydrogen embrittlement of high strength β-titanium alloys such as STA LCB and Ti-15-3 at 25°C. From a scientific perspective, this work aims to understand how and why hydrogen damage occurs in this class of materials.

Specific hydrogen embrittlement objectives include:

- Develop a calibration relationship between electrochemical cathodic-current density and total dissolved hydrogen content for STA LCB and Ti-15-3 sheet, with emphasis on the low hydrogen concentration regime. Examine the role of the surface oxide, in both hindering hydrogen uptake at low current densities and blocking hydrogen loss during fracture experiments.
- Improve the resolution and long-term stability of the direct current potential difference method, specifically for thin-sheet β-titanium alloy specimens subjected to slow loading rates and cryogenic to mildly elevated temperatures that may promote internal hydrogen embrittlement.
- Determine the hydrogen concentration dependence of both the threshold stress intensity and subcritical crack growth rates characteristic of internal hydrogen embrittlement of STA

LCB and Ti-15-3 sheet. Emphasize the critical amount of hydrogen necessary for embrittlement, particularly in the low to moderate hydrogen concentration range.

- Determine the microscopic processes of hydrogen embrittlement, with emphasis on establishing the controlling microstructural features.

It is necessary to understand ductile fracture as a basis for investigating the effects of dissolved hydrogen. Alloy fracture toughness must be sufficiently well characterized and high to provide a basis to determine the extent of any deleterious hydrogen affect. Toughness variability must be understood to guarantee that differences in fracture resistance are related to hydrogen rather than microstructure-induced variability. Ductile fracture modes must be characterized in order to determine which modes are affected by the presence of dissolved hydrogen. It is not necessary to develop a comprehensive understanding of all ductile fracture mechanisms, but rather only those that will provide insight in understanding the hydrogen-damage mechanism. Specific objectives include:

- Characterize the initiation fracture toughness and K *vs* Δa resistance curves of STA LCB and Ti-15-3 sheet at 25°C.
- Define the mechanisms for ductile fracture of STA and LCB sheet.
- Determine if the initially high dissolved hydrogen content of LCB sheet affects fracture toughness.

Approach

Fracture Mechanics

Recent work at UVa has shown that fracture mechanics can be applied to characterize and understand the time-temperature dependent fracture behavior of advanced elevated temperature aluminum alloys.[11-14] These methods will be employed for testing titanium alloys, with the most significant differences in the test setup arising from the substantial increase in electrical resistivity of titanium compared to aluminum, coupled with the significantly reduced thickness of the compact tension (CT) specimens.

The experimental method is based on the rising crack mouth opening displacement R-curve approach. A computerized system measures load, crack mouth opening displacement, and crack length (from direct current electrical potential of the sample and adjusted by a reference probe) as

a function of time for a fatigue precracked CT specimen mounted in a closed-loop servoelectric test machine and operated under constant actuator-displacement control. These data are analyzed to yield the R-curve, represented in terms of elastic-plastic J-integral (J) versus crack extension, Δa. This technique yields values of the initiation fracture toughness (K_{IC}, K_{ICi}, K_{JICi}, and K_{JIC}) and the plane stress tearing resistance with a single fracture mechanics specimen.[14] In addition, when stable cracking occurs, J-Δa can be analyzed to yield K versus crack growth rate, da/dt. Sheet CT specimens are 1.7 mm thick and 76.2 mm wide, and are restrained with face plates to prevent buckling.

Considering the effect of hydrogen on the rising-CMOD R-curve, two variables are of prime interest for precharged specimens; the loading rate and total dissolved hydrogen concentration. The applied fixed-CMOD rate will be varied such that tests last from minutes to one week.

Hydrogen Embrittlement

A main goal of this research is to understand the effect of lattice-dissolved and microstructure-trapped hydrogen on the onset and subsequent stable growth of cracks in high strength metastable β-titanium alloys. CT specimens are precharged electrochemically with target hydrogen concentrations between 100 and 1000 wppm. In this technique, the specimen is immersed and polarized cathodically in a solution of 10 ml sulfuric acid, 1000 ml water, and 0.8 g $Na_4P_2O_7$ at 90°C for a sufficient time (typically 96 hours) to insure a uniform hydrogen concentration through the thickness of the specimen.

The main experimental challenge is to destabilize the otherwise protective oxide film to permit hydrogen uptake. It may be difficult to produce low hydrogen concentrations because the over-potential necessary to reduce TiO_2 may be sufficiently high and produce dissolved hydrogen levels in excess of 500 to 1000 wppm. Low over-potentials, necessary for low hydrogen levels, may be insufficient to reduce the oxide film and to enable hydrogen entry. If this turns out to be the case, then it will be necessary to destabilize the hydrogen-barrier passive film by chemical or mechanical means.

RESULTS

Materials

Two metastable β-titanium alloys, processed in sheet form, were selected for this study.

Compositions are listed in Table I, as specified by the vendor. For both alloys, the hydrogen level was measured, as the total dissolved hydrogen concentration, by LECO using a melt extraction technique.

Table I: Alloy Compositions (wt. pct.)

Alloy	Ti	Mo	Fe	Al	Nb	O	V	Cr	Sn	H
TIMETAL LCB	Bal.	6.8	4.5	1.5	---	0.09	---	---	---	0.00236
TIMETAL 15-3	Bal.	---	0.16	3.1	---	0.105	15	3	3	0.00044

LCB sheet was processed thermomechanically by TIMET and according to the following procedures:

19.05 cm diameter x 25.4 cm long ingot
Beta forge to 10.16 cm x 15.24 cm from 1093°C
Alpha/Beta forge to 4.45 cm x 16.5 cm from 760°C
Beta roll to 0.51 cm x 16.51 cm from 849°C
Alpha/Beta roll to 0.31 cm x 16.51 cm from 752°C
Cold roll to 0.18 cm (42% reduction)
Alpha/Beta solution treat at 760°C for 20 minutes
Fan air cool
Age at 593°C for 20 hours

The mechanical properties of TIMET LCB sheet CT specimens, tested to date, are summarized in Table II. Hardness was measured on each specimen and ultimate tensile strength (σ_{UTS}) was determined from a correlation of hardness with σ_{UTS}, developed for LCB sheet of 1.6 mm thickness. The equation for this correlation is:

$$\sigma_{UTS} = 5.49 * Hardness - 47.69 \quad \textbf{(1)}$$

where σ_{UTS} is in units of ksi and hardness in Rockwell C-scale.[15] These predicted ultimate tensile strengths for LCB sheet agree well with those measured at UVa by Kazanjian which averaged 1176 MPa.

Table II: TIMET LCB Mechanical Properties

Specimen Identification	Hardness (Rockwell C)	Ultimate Tensile Strength (MPa)
Sheet 4	40.2	1193
Sheet 6	40.7	1212
Sheet 7	40.8	1216
Sheet 9	41.5	1242
Sheet 10	41.5	1242
Sheet 12	40.7	1212
Sheet 13	39.9	1181
Sheet 15	39.7	1174
Sheet 16	40.3	1197
Sheet 17	40.4	1200
Sheet 18	40.2	1193

Ti-15-3 sheet, 2.0 mm thick, was obtained from TIMET during this reporting period. The sheet microstructure consisted of recrystallized equiaxed (32 to 34 μm diameter) β grains without α precipitation, consistent with the β-solution treated condition of this alloy. A heat treatment will be selected for Ti-15-3 to produce yield strengths comparable to STA LCB.

Direct Current Potential Difference (dcPD) Test Methodology

The rising CMOD R-curve test methodology has been improved by: (a) electrically isolating the specimen from the load train, (b) improving the bit-resolution of the analog to digital processor, (c) programming new PC software for data acquisition, and (d) implementing a reference probe. These changes collectively reduced the short-term noise in the dcPD signal to ±0.1% of the base signal, and critically, eliminated long term signal drift that obscured crack initiation and growth monitoring.

The reference probe approach was implemented to reduce long-term and spurious variations in the measured dcPD signal. This technique uses a second LCB sheet CT specimen, situated in close proximity to the CT sample being tested and connected to the power supply in series with the

fracture sample. The direct current potential difference of the reference probe is measured at the same time as that of the fracture sample being tested. The reference probe should eliminate variation in sample dcPD which may be due to temperature or applied current fluctuations.

Figures 1 and 2 show the evolution of data from replicate four-hour rising CMOD tests of STA LCB CT specimens at room temperature using the improved system described above. Part (a) of each figure shows uncorrected cracked-sample dcPD versus crack mouth opening displacement (CMOD). Uncorrected sample dcPD refers to the electrical potential difference measured from the sample, with thermoelectric potentials eliminated by periodically reversing the polarity of current flowing through the CT specimen. The CMOD-dependence of this dcPD signal is different for each specimen, as shown by the results for Sheet 17 and 18.

Crack-growth initiation is indicated by a rise in measured electrical potential difference because the electrical resistance of a cracked body increases as the crack extends. The definition of crack-growth initiation is complicated, however, by rises or declines in dcPD which mask initiation; such complications are evident in Figures 1(a) and 2(a). In both tests there was an initial small increase in the uncorrected sample dcPD as load increased. This is typical in rising CMOD tests and is associated with the separation of fatigue precrack surfaces which contacted at low load. Ideally, the plot of uncorrected sample dcPD vs CMOD would then remain horizontal until initiation, at which point the dcPD signal would rise steadily. However, this is not the case, as demonstrated in Figures 1 and 2.

The data from Sheet 18 in Figure 2(a) show an initial increase in uncorrected sample dcPD, followed by a steady rise. It is possible to define crack-growth initiation as the point where the uncorrected sample dcPD signal first increases above the mildly rising linear portion of these data. However, it is not possible to define initiation based on the uncorrected sample dcPD data for Sheet 17, Figure 1(a). As this plot shows, uncorrected dcPD values decreased steadily by nearly 20 μV before the signal began to increase. This downward trend masks crack initiation. This phenomenon was encountered typically in early testing of titanium sheet CT specimens and led to the implementation of the reference probe.

Parts (b) of Figures 1 and 2 show data from the same rising CMOD R-curve tests, with each uncorrected sample dcPD value adjusted using the reference probe. The equation used to define this true dcPD (V_{True}) at any time, t, is:

$$V_{True} = V_{Uncorrected}\left(\frac{V_{Ref,o}}{V_{Ref}}\right) \quad (2)$$

where V_{Ref} is the reference probe dcPD signal at time t, and $V_{Ref,o}$ is the initial reference probe potential, both of which were corrected for thermoelectric potentials.[16]

Load versus CMOD is also plotted in Figures 1(b) and 2(b) to clarify where crack-growth initiation occurs. Deviation from linearity in load versus CMOD is explained by plasticity and/or by crack growth initiation. As will be shown, there is limited plasticity in these high strength titanium alloy specimens, therefore the non-linearity in these plots is due to crack growth. Examination of these plots reveals that the onset of nonlinearity in load versus CMOD occurs at approximately the CMOD where the adjusted sample dcPD begins to increase above a linearly rising baseline.

Crack-growth initiation was defined quantitatively using the measurements of V_{True} *vs* CMOD and load *vs* CMOD. An estimated crack mouth opening displacement (CMOD*), where V_{True} *vs* CMOD changes slope, was used as a reference point for linear regression. Baseline V_{True}-CMOD data (before crack growth) are fit by linear regressions from 0.6 to 0.9 CMOD*, and crack growth data are fit from 1.1 to 1.4 CMOD*. The intersection of the two linear fits indicates crack-growth initiation and is labeled $CMOD_i$ in Figures 1(b) and 2(b). This method of determining crack-growth initiation is an adaptation of the technique developed by Haynes and Gangloff.[14]

Figures 1(c) and 2(c) show the K-Δa curves for these rising CMOD tests. Crack length was determined from the dcPD signal and a calibration relationship given by the following expression:

$$\frac{a}{W} = -0.5051 + 0.8857\left(\frac{V}{V_o}\right) - 0.1398\left(\frac{V}{V_o}\right)^2 + 0.0002398\left(\frac{V}{V_o}\right)^3 \quad (3)$$

where a is the calculated crack length, W is CT specimen width, V (actually V_{True}) is the dcPD at any time, t, and V_o is the dcPD at a/W = 0.241. V_o is calculated from the measured V_{True}, coupled with the measured fatigue precrack length, at the identified point of crack-growth initiation (Δa = 0).[16] Crack extension was defined as Δa = 0.0 for all points less than or equal to the defined initiation point. These plots show that there is good agreement in the appearance of the R-curves for the replicate experiments.

Specific fracture toughness parameters are determined from R-curves of the type presented in Figures 1(c) and 2(c). For a steeply rising R-curve typical of sheet specimens, it is necessary to carefully define the crack initiation point, and to consider multiple definitions of initiation toughness. For example, a 1 μV difference in the selected initiation-dcPD value can affect K_{JICi} by up to 10 MPa√m, as discussed in the next section.

As-Received Fracture Toughness

The rising CMOD R-curve test method was used to determine the fracture toughness of TIMET LCB sheet CT specimens at room temperature, and without prior hydrogen introduction. The results of these tests are summarized in Table III. The average hydrogen concentration for as-received specimens (A.R.) is 236 wppm.

Table III: TIMET LCB Fracture Toughness at 23°C

Specimen	Hydrogen (wppm)	J_{IC} (kJ/m^2)	K_{JIC} (MPa√m)	J_{ICi} (kJ/m^2)	K_{JICi} (MPa√m)	K_{ICi} (MPa√m)
Sheet 4*	A.R.	34.5	66.0	28.1	59.6	59.7
Sheet 6*	A.R.	49.9	79.9	18.3	48.4	48.5
Sheet 7*	A.R.	40.5	72.0	21.0	51.9	52.0
Sheet 15*	A.R.	33.4	64.2	24.9	55.4	55.4
Sheet 16	A.R.	32.7	64.0	13.1	40.6	40.6
Sheet 17	A.R.	23.0	54.0	9.7	34.9	34.9
Sheet 18	A.R.	25.5	56.7	12.2	39.1	39.1
Sheet 13	335	43.8	76.1	25.4	58.0	58.0
Sheet 12	770	1.3	11.9	0.9	10.7	10.8
Sheet 9	871	1.5	12.5	1.2	11.8	11.8
Sheet 10	1150	0.9	9.8	0.8	9.8	9.8

Specimens identified by an asterisk were tested before the crack length monitoring system was improved, and the associated fracture toughnesses within the shaded blocks are of questionable accuracy. The three tests with Sheets 16, 17, and 18 were based on the new method with improved dcPD stability and analysis of crack initiation. Sheets 9 through 13 were hydrogen precharged

electrochemically, then fractured by the rising load CMOD method. Electrical potential data were obtained with the early version of the test system for the hydrogen experiments.

The initiation fracture toughness parameters (J_{IC}, K_{JIC}, J_{ICi}, and K_{JIC}) were determined from K-Δa data of the sort shown in Figures 1 and 2. The subscript (i) in three columns denotes that crack-growth initiation was detected by the regression-resolved increase in dcPD, while J_{IC} and K_{JIC} were based on ASTM Standard E-1152 and a 0.2 mm offset blunting line. Elastic-plastic J was calculated from the load, load-line displacement, and crack length data points at initiation using a calculated-compliance area method. J was converted to a linear elastic stress intensity by the following relation:

$$K = \left(\frac{JE}{1-\nu^2} \right)^{1/2} \tag{4}$$

K_{JICi} was determined from measured J_{ICi} and K_{JIC} from measured J_{IC}. K_{ICi} is the linear elastic fracture toughness based on the K-solution given in ASTM Standard E-399 which is:

$$K_{ICi} = \left(\frac{P_i}{BW^{1/2}} \right) f\left(\frac{a_i}{W} \right) \tag{5}$$

where P_i and a_i are the load and crack length at initiation, and B and W are specimen thickness and width, respectively. Unlike ASTM Standard E-399 (K_{IC}) which is based on a secant offset method to determine crack-growth initiation, K_{ICi} is based on a resolvable increase in dcPD.

The values of K_{ICi} and K_{JICi} for all LCB specimens in Table III are approximately equal (to within ±0.1 MPa). Both values were determined based on dcPD-detected crack-growth initiation, with the only difference arising from the method of calculating K. Recalling that J_{Total} has both elastic and plastic components, J-integral calculations indicate that the plastic contribution ($J_{Plastic}$) to J_{Total} is insignificant compared to the elastic contribution ($J_{Elastic}$); small scale yielding is maintained and linear-elastic K analysis is sufficient.

The data in Table III reveal interesting aspects of the rising CMOD R-curve fracture resistance of STA LCB sheet. For both old and new experiments with A.R. LCB specimens, initiation fracture toughness, determined by true dcPD, is consistently lower than K_{JIC} determined using ASTM Standard E-1152. This difference is due to the fact that dcPD detects finer microstructural damage than the amount of damage present at the intersection of the offset blunting

line and J-Δa curve. This difference is pronounced for thin sheet specimens, where the R-curve may rise due to both intrinsic plane strain fracture resistance as well as increasing plane stress constraint.

The initiation fracture toughness values determined using the improved acquisition system and reference probe are consistently lower than previously reported values; Table III.[17-18] For example, K_{JICi} values for the three most recent tests (40.6, 34.9, and 39.1 MPa$\sqrt{m}$) are significantly lower than previously reported values, which ranged from 48.4 to 59.6 MPa$\sqrt{m}$ (shaded cells). This behavior is seen when comparing any of the fracture toughness parameters in Table III. Variability in the dcPD signal likely obscured initiation in earlier tests; the toughness parameters represented by the shaded blocks and marked by * in Table III are not necessarily accurate. These experiments must be reanalyzed, utilizing a compliance method described below, to produce high-resolution initiation fracture toughnesses consistent with K_{JICi} determined using the improved dcPD acquisition system. Because of the poor dcPD signal, full K *vs* Δa R-curves and blunting-line offset K_{JIC}-type values cannot be calculated for these earlier experiments.

It is necessary to establish the magnitude and consistency of the percent deviation from linearity in load *vs* CMOD at dcPD-determined crack-growth initiation for the recent improved tests so that the experiments without a reference probe can be reanalyzed. Figure 3 shows percent deviation from load *vs* CMOD linearity, and V_{True} *vs* CMOD for Sheets 17 and 18. The crack mouth opening displacement at dcPD-based initiation ($CMOD_i$) is labeled and the corresponding percent deviation from the linear load fit is determined. This percent difference is 0.3 and -0.2% for specimens 17 and 18, respectively, suggesting that both compliance and dcPD provide a consistent definition of the early stage of crack tip process zone damage. Based on these results, the point at which the deviation from load *vs* CMOD linearity first begins to rise above zero is defined as crack-growth initiation.

The compliance analysis was used to reanalyze the previous fracture toughness experiments with A.R. LCB (shaded cells in Table 3), and the results are listed in Table IV. The linear-elastic stress intensities in Table IV were calculated using Equation 5, the load corresponding to the onset of deviation from load-CMOD linearity, and the measured fatigue precrack length. These values are significantly less than the previously reported initiation toughnesses, and are in good agreement with the values determined using the improved crack length monitoring system.

Table IV: Compliance-based Initiation Fracture Toughnesses

Specimen Identification	K_{JICi} (MPa$\sqrt{m}$)
Sheet 4	27.4
Sheet 6	32.0
Sheet 7	34.1
Sheet 15	35.5

Precise definition of crack initiation toughness remains elusive because of uncertainties in both the compliance and dcPD methods. For example, agreement between the two methods is not perfect for Sheet 18 (Figure 3(b)); a positive compliance change does not occur until the applied CMOD is somewhat higher than $CMOD_i$. As a second example, Figure 4 shows data from a four-hour rising CMOD test for Sheet 16, using the improved crack length monitoring system. Variable V_{True} obscured definition of $CMOD_i$, and the value was atypically greater than CMOD*. In addition the first positive deviation from load-line linearity occurred well below CMOD* and $CMOD_i$, and the deviation at $CMOD_i$ was large (~6%). The initiation point determined from the compliance-based method is labeled δ^* in Figure 4(b). Two R-curves were generated for this specimen, based on dcPD (Figure 4(c)) and compliance (Figure 4(d)). While the values of K_{JICi} were very different, 40.6 (dcPD from Figure 4(b)) and 24.6 MPa$\sqrt{m}$ (compliance), the two R-curves in Figure 4 are similar, as are values of offset-blunting line K_{JIC} for dcPD-detected and compliance-based initiation were 64.0 and 61.7 MPa$\sqrt{m}$, respectively.

Experiments were conducted to prove that the high resolution dcPD and compliance methods accurately portray crack tip damage and crack growth initiation. A CT specimen was fatigue precracked, and a rising CMOD R-curve test was interrupted when true dcPD suggested that initiation occurred. The crack was then extended by fatigue to mark the fracture surface and enable the same CT specimen to be used for several interrupted tests at progressively higher K levels. Finally, the rising CMOD test was run to completion to develop a full R-curve and the crack growth initiation parameters (K_{JIC} and K_{JICi}). The fracture surface was examined by SEM to determine the amount of ductile crack growth at each K level. The K_{JICi} for this specimen was 39.1 MPa$\sqrt{m}$, as reported in Table III for Sheet 18. The rising CMOD tests were interrupted at the K-

levels shown in Table V. This table also shows the measured crack extension, associated deviation from load-CMOD linearity, ratio of V_{True} at interruption to true sample dcPD at initiation, and predicted crack growth from Equation (3). These results show that actual crack growth occurs without being detected by either the dcPD or compliance methods. Of these two, dcPD is a more sensitive technique for detecting crack initiation, with the initiation point corresponding to between 100 and 175 μm of ductile crack extension.

Table V: Measured and Predicted Crack Lengths

K at interrupt (MPa√m)	Measured Δa (mm) (1)	ΔP-CMOD (%)	V/V_o	Predicted Δa (mm)
27.5	0	0	1	0
34.4	0.102	0	1	0
39.9	0.173	0	1.0021	0.097
51.2	0.250	2.5	1.0037	0.134

(1) Because cracking was irregular across the specimen width, crack length was determined by dividing the area of ductile crack extension by specimen width.

Figure 5 shows the R-curves for the three replicate rising CMOD tests based on dcPD-detected initiation (Figures 2 and 4), the SEM-based data from the four interrupted tests (Table V), and the offset blunting line used to determine K_{JIC}. Crack-growth clearly initiates in STA LCB at levels well below K_{JIC}. Measured crack lengths from the interrupted tests agree reasonably with the R-curves from the replicate tests using the improved dcPD method. The interrupted test data are offset from the R-curves by approximately 100 μm, as indicated by the arrows in the figure, suggesting that dcPD-detected K_{JICi} corresponds to the stress intensity required to produce 100 μm of crack extension. This comparison validates K_{JICi} from dcPD.

Figure 6 shows initiation fracture toughness (K_{JIC}) *vs* ultimate tensile strength (UTS) for STA LCB sheet, as well as for STA Beta-21S sheet processed in different ways.[15] The initiation fracture toughnesses for LCB are based on a 0.2 mm offset blunting line rather than dcPD-detected initiation to be consistent with the values reported for Beta-21S. The LCB data are described by a box since UTS values were from hardness measurements and differed from measured values by up to 70 MPa. Only the results from the three most recent tests are shown, and they are similar to

the lower bound for the Beta-21S sheet data. The higher K_{JIC} values for LCB which were reported previously[17-18] are not included because of the noisy dcPD signal associated with these tests. Process zone damage, as detected by dcPD and verified by interrupted rising CMOD tests, occurs at stress intensities of 27 to 40 MPa$\sqrt{m}$, and is marked as a reference on this plot.

Several points are apparent based on the experiments conducted during this reporting period: (1) K_{JIC} for A.R. LCB is between 54 and 64 MPa$\sqrt{m}$, and is not outstanding, (2) crack growth occurs at values of K_{JICi} that are well below K_{JIC}, and K-levels at the onset of initial crack growth are difficult to measure, reproducibly, (3) the data in Tables 3 and 4 and Figures 4(c) and 4(d) suggest that an average value for K_{JICi} is 33.5 MPa$\sqrt{m}$, (4) microscopic crack growth ensues at K levels somewhat below K_{JICi} from the high resolution dcPD and compliance methods, and (5) the full K-Δa R-curve must be considered for hydrogen embrittlement studies. These results provide the basis for examination of the effect of dissolved hydrogen on the fracture resistance of STA LCB.

Hydrogen Charging

Specimens are being hydrogen charged prior to loading to examine the susceptibility of high strength β-titanium alloys to internal hydrogen embrittlement during rising CMOD. Titanium alloys are particularly difficult to hydrogen charge, and substantial development work is required to be able to introduce controlled modest hydrogen levels to alloys such as LCB and Ti-15-3.

Hydrogen precharging experiments are being conducted with LCB to determine the critical parameters and better establish the calibration relationship between applied cathodic current density and total dissolved hydrogen concentration. Figure 7 shows a plot of total hydrogen concentration (C_H) *vs* cathodic current density (i_C) on log-log axes for STA LCB sheet specimens that were surface treated and H-charged electrochemically in an elevated temperature acidic solution. Initial data from CT specimens, H-charged without surface preparation, were variable and are not included in this plot. Surface treatment, specifically glass bead blasting or mechanically grinding, before electrochemical charging reduces variability in hydrogen uptake during charging. This may be due to removal of non-uniform and thick oxide layers which are present from elevated temperature sheet processing.

The data in Figure 7 are described by two trend lines. Hydrogen concentration is essentially equal to the as-received level (horizontal dashed line) and is independent of increasing cathodic current density until approximately 0.15 mA/cm^2. Above this current density, total

hydrogen concentration increases rapidly with increasing i_C. The regression fit to the data for cathodic current densities greater than 0.15 mA/cm^2 yields a slope of 0.7. This value is ideally 0.5, as suggested by electrochemical consideration of cathodic hydrogen production and uptake ($C_H \propto \sqrt{i_C}$).

This behavior can be explained by two factors. Surface oxides are more stable at higher (less negative) potentials, which correspond to lower current densities, and the presence of such an oxide prevents hydrogen uptake. It may be necessary to exceed a critical current density, above which the surface oxide is rendered unstable, to enable hydrogen uptake. The higher cathodic overpotential, necessary to destabilize the blocking oxide, produces an unacceptably large hydrogen concentration. Additionally, the surface hydrogen concentration in equilibrium with low current density may be less than the as-received level in LCB. While hydrogen egress should occur for this case, it may be blocked by the surface oxide. Again, a critical cathodic current density must be exceeded to establish a surface concentration of hydrogen in excess of the relatively high level present in as-received LCB, and depending on surface oxide state.

Charging experiments are in progress to better establish the calibration relationship, particularly in the cathodic current density range of 0.05 to 0.25 mA/cm^2. The cell was modified to minimize solution loss due to evaporation. LCB specimens were charged in the improved cells, but LECO analysis results are pending. The solution to the barrier oxide problem may be to increase the solution acidity to destabilize the protective oxide, then to apply low overpotentials to produce the desired low hydrogen concentrations. If the solution temperature is decreased, it will be possible to use a reference electrode to monitor the time required to destabilize the surface film before cathodic polarization. This avenue is being examined.

The data in Table VI were generated to prove that hydrogen is retained without loss, from the time the CT specimen is charged and the rising CMOD test is initiated, until hydrogen content analysis. A sample was electrochemically charged at 0.25 mA/cm^2, sectioned, and exposed in moist air for the times and temperatures shown before hydrogen analysis. Samples were shipped for LECO analysis in dry ice to prevent hydrogen loss. The results shown in Table VI (and plotted in Figure 7) demonstrate that no hydrogen loss occurred for at least 19 days at temperatures of 75°C and 48 days at 25°C. This behavior is most likely due to the hydrogen barrier property of the surface oxide, and will enable accurate hydrogen embrittlement experiments without hydrogen loss.

Table VI: Hydrogen Loss During Moist Air Exposure

	Exposure Temperature	
Exposure Time (hrs)	25°C (wppm)	75°C (wppm)
As charged - 0	1376, 1711	1376, 1711
168	--	1373
456	1441	1811
1152	1335	--

Hydrogen Embrittlement

Predissolved hydrogen, in concentrations greater than approximately 500 wppm, significantly embrittles STA LCB sheet, reducing initiation fracture toughness parameters to a small fraction of the as-received air fracture toughness and promoting subcritical crack growth. Data in Table III show this, while Figure 8 shows R-curves for two LCB sheet CT specimens tested at the same load-line displacement rate but with different hydrogen concentrations. The R-curve for the hydrogen-charged specimen (Sheet 10, 1150 wppm H) is markedly reduced compared to that of the as-received specimen (Sheet 18, 236 wppm H). Crack-growth initiation in the H-charged microstructure occurs at a significantly reduced K level compared to the behavior of the as-received specimen. This low threshold stress intensity (K_{TH} = 9.8 MPa$\sqrt{m}$) is well below K_{JICi} and K_{JIC} for the lower hydrogen case in Figure 8, and detailed previously in Figures 1 through 6. In addition, the as-received specimen requires increasing K levels to propagate the crack, while the R-curve for the precharged specimen is horizontal, indicating that stable crack growth occurs at a constant K level. K_{TH} results for two intermediate hydrogen levels are presented in Table VII, and confirm the embrittling effect of predissolved hydrogen.

Figure 9 shows crack length versus time for the two tests represented in Figure 8. This figure clearly shows the increased crack growth rate (da/dt about 100-times greater) for the hydrogen precharged specimen relative to the as-received case. This trend is supported by the data in Table VII, which show the crack growth rates for various rising CMOD tests. Crack growth rate increases dramatically with increasing predissolved hydrogen concentration, and the magnitude of da/dt appears to increase with increasing dissolved hydrogen concentration at 25°C.

Table VII: Crack Growth Rate in STA LCB with Varying Hydrogen Levels at Fixed CMOD Rate

Hydrogen Concentration (wppm)	K_{TH} (MPa$\sqrt{m}$)	da/dt (mm/sec) [5]
As Received (236)	34.1 (K_{JICi})	8.1×10^{-5}
	35.2 (K_{JICi})	1.0×10^{-4}
	39.8 (K_{JICi})	1.0×10^{-4}
770	10.7	1.8×10^{-3}
871	11.8	5.8×10^{-3}
1150	9.8	1.0×10^{-2}

Figure 10 shows the ratio of threshold stress intensity for hydrogen cracking to initiation fracture toughness in air *vs* total hydrogen concentration for STA β-titanium alloys fractured by slow rising CMOD loading rate. The data for LCB sheet were generated under plane strain constraint and defined by an offset blunting line (K_{JIC}), and hydrogen concentration was varied using the electrochemical charging technique. The results for Beta-21S and Ti-15-3 were produced by a separate study at UVa, with plate microstructures, and were based on an approximate secant offset method to determine crack-growth initiation at K_{IC}.

The critical hydrogen concentration ($C_{H\text{-}Crit}$) necessary to trigger internal hydrogen embrittlement is defined as the hydrogen concentration that reduces the threshold stress intensity to 25 percent of the air fracture toughness. $C_{H\text{-}Crit}$ appears to be significantly lower for STA LCB sheet than for other high strength β-titanium alloys tested. The solid line shows the trend of K_{TH}/K_{IC} with total hydrogen concentration for Beta-21S and Ti-15-3 plate, while the dashed lines show the trend and uncertainty for STA LCB sheet. Based on current data, the apparent critical hydrogen concentrations for STA Beta-21S and Ti-15-3 plate microstructures are about 1200 wppm, while the value for STA Timet LCB sheet appears to be 700 wppm or less.

Data for the low hydrogen concentration region are limited and other interpretations are

---

5 To calculate da/dt, a line was fit to the initial 0.5 mm of crack growth data for each A.R. specimen. This segment of cracking was approximately linear, while crack length accelerated somewhat at higher K levels. Crack length *vs* time data are approximately linear for all hydrogen-charged specimens over the entire stress intensity range examined.

possible. For example, K_{TH}/K_{IC} for Ti-15-3 may be well-described by the sloped-dashed line drawn for LCB. With this interpretation, $C_{H\text{-}Crit}$ would be near 700 wppm, similar to STA LCB. In order to better examine the effect of alloy composition and microstructure, the hydrogen embrittlement resistance of Ti-15-3 sheet microstructure will be characterized, as well as more accurately determining $C_{H\text{-}Crit}$ for STA LCB sheet.

Figure 11 shows the ratio of threshold stress intensity for hydrogen cracking to initiation fracture toughness in air *vs* total hydrogen concentration for STA LCB sheet alloys fractured by slow rising CMOD loading. Fracture thresholds are supplemented with fractographs of each crack surface. In all fractographs crack propagation occurs from bottom to top. In the as-received condition (236 wppm H), STA LCB specimens appeared to fail predominantly by dimpled rupture, while at higher hydrogen concentrations (770 wppm), the failure was transgranular with the threshold stress intensity reduced to only 30% of the air fracture toughness. At an intermediate hydrogen concentration (335 wppm), the threshold stress intensity was not reduced relative to the air fracture toughness, but there were both high toughness features (dimples) as well as low toughness features (transgranular failure). These data and fractographs suggest that $C_{H\text{-}Crit}$ for LCB sheet lies between 335 and 770 wppm H for the slow loading rate used. A change in loading rate or temperature could shift $C_{H\text{-}Crit}$ to lower or greater values.

Conclusions

- Direct current potential difference is an effective technique for detecting crack growth initiation, as well as a significant portion of the stable crack growth R-curve for compact tension specimens of high strength β-titanium alloys. Care must be taken to eliminate spurious voltages that are pronounced for thin sheet β-titanium and to carefully define the point of crack growth initiation. The full K-Δa R-curve must be considered as a basis for hydrogen embrittlement studies.
- K_{JIC} for STA LCB without hydrogen exposure is between 54 and 64 MPa√m, and is not outstanding compared to other high strength β-titanium alloys. Crack growth occurs at values of K_{JICi} that are between 27 and 40 MPa√m, with an average value of 33.5 MPa√m based on high resolution electrical potential and compliance measurements.
- DcPD-detected crack-growth initiation (K_{JICi}) corresponds to approximately 100 μm of crack extension in LCB sheet CT specimens. This initial stage of crack advance is irregular

on the microstructural scale.

- Compliance data from tests with uncorrected and variable dcPD signals can be analyzed to estimate initiation fracture toughness values consistent with the improved dcPD R-curve methodology.
- The surface oxide on β-titanium alloys hinders hydrogen uptake and complicates the introduction of low hydrogen concentrations that are critical to applications of these alloys.
- Dissolved hydrogen introduced during electrochemical precharging is not lost during prolonged fracture testing and subsequent analysis.
- Predissolved hydrogen significantly reduces the initiation fracture toughness, increases crack growth rate, and alters the fracture modes of high strength β-titanium alloys.
- A threshold hydrogen concentration is necessary to trigger embrittlement in high strength β-titanium alloys and varies for each alloy system. This critical hydrogen concentration appears to be less than 800 wppm for STA LCB.

Future Work

The goals of future work are to:

- Improve the hydrogen charging calibration relationship for STA LCB and Ti-15-3 sheet, with emphasis on a method to reproducibly produce low hydrogen concentrations between 100 and 1000 wppm.
- Decrease the anomalously high hydrogen concentration in as-received STA LCB to approximately 50 wppm. This high hydrogen concentration may complicate the calibration relationship and embrittle as-received specimens.
- Precisely determine $C_{H\text{-}Crit}$ for STA LCB sheet at room temperature and a constant slow loading rate.
- Characterize the microstructure and ductile fracture resistance of as-received STA Ti-15-3 sheet as a basis for investigating the effects of microstructure and hydrogen on fracture resistance.
- Investigate the fracture resistance of solution treated and aged Ti-15-3 sheet as a function of hydrogen concentration.
- Define the microscopic modes of ductile fracture and hydrogen embrittlement in STA LCB and Ti-15-3 sheet.

References

1. G. Terlinde, T.W. Duerig, and J.C. Williams, "Microstructure, Tensile Deformation, and Fracture Toughness in Aged Ti-10V-2Fe-3Al", Metallurgical Transactions A, Vol. 14A p. 2101, 1983.

2. G. Terlinde and K.-H. Schwalbe, "The Role of α-Phase in the Fracture Toughness and Tensile Fracture of an Aged, Metastable β-Ti-Alloy", in Microstructure Fracture Toughness and Fatigue Crack Growth Rate in Titanium Alloys, AK Chakrabarti and J.C. Chestnut, eds., TMS-AIME, Warrendale, PA, p. 97, 1987.

3. T.W. Duerig and J.C. Williams, "Overview: Microstructure and Properties of Beta Titanium Alloys", in Beta Titanium Alloys in the 80's, R.R. Boyer and H.W. Rosenberg, eds., TMS-AIME, Warrendale, PA, p. 19, 1984.

4. F.H. Froes, J.C. Chestnutt, C.G. Rhodes, and J.C. Williams, "Relationship of Fracture Toughness and Ductility to Microstructure and Fractographic Features in Advanced Deep Hardenable Titanium Alloys", in Toughness and Fracture Behavior of Titanium ASTM STP 651, American Society for Testing and Materials, Philadelphia, PA, p. 115, 1978.

5. D. Eylon, A. Vassel, Y. Combres, R.R. Boyer, P.J. Bania and R.W. Schutz, "Issues in the Development of Beta Titanium Alloys", J. of Metals, July, p. 14, 1994.

6. G.A. Young and J.R. Scully, "Effects of Hydrogen on the Mechanical Properties of a Ti-Mo-Nb-Al Alloy", Scripta Metal., Vol. 28, p. 507, 1993.

7. G.A. Young and J.R. Scully, "Hydrogen Embrittlement of Solution Heat-Treated and Aged β-Titanium Alloys Ti-15%V-3%Cr-3%Al-3%Sn and Ti-15%Mo-3%Nb-3%Al", Corrosion, Vol. 50, No. 12, p. 919, 1994.

8. G.A. Young and J.R. Scully, "The Effects of Hydrogen on the Room Temperature Mechanical Properties of Ti-15V-3Cr-3Al-3Sn and Ti-15Mo-3Nb-3Al", in Beta Titanium Alloys in the 1990's, D. Eylon, R.R. Boyer and D.A. Koss, eds., TMS-AIME, Warrendale, PA, p. 147, 1993.

9. M.A. Gaudett and J.R. Scully, "Hydrogen Interactions and Embrittlement in Metastable Beta Ti-3Al-8V-6Cr-4Mo-4Zr", in Hydrogen Effects in Materials, A.W. Thompson and N.R. Moody, eds., TMS-AIME, Warrendale, PA, p.745, 1996.

10. M.A. Gaudett, "Hydrogen Interactions and Embrittlement in Metastable Beta Ti-3Al-8V-6Cr-4Mo-4Zr", Ph.D. Dissertation Proposal, University of Virginia, Charlottesville, VA, 1996.

11. W.C. Porr, Jr. and R.P. Gangloff, "Elevated Temperature Fracture of RS/PM Alloy 8009: Part I. Fracture Mechanics Behavior", Metallurgical Transactions A, Vol. 25A, p. 365, 1994.

12. B.P. Somerday, Yang Leng and R.P. Gangloff, "Elevated Temperature Fracture of Particulate-Reinforced Aluminum Part I: Fracture Toughness", Fatigue Fract. Engng Mater. Struct., Vol. 18, No. 9, p.1031, 1995.

13. S.S. Kim, M.J. Haynes and R.P. Gangloff, "Localized Deformation and Elevated-Temperature Fracture of Submicron-Grain Aluminum with Dispersoids", Materials Science and Engineering A203, p. 256, 1995.

14. M.J. Haynes and R.P. Gangloff, "High Resolution R-Curve Characterization of the Fracture Toughness of Thin Sheet Aluminum Alloys", Journal of Testing and Evaluation, Vol. 25, No. 1, p. 82, 1996.

15. HSR Metallic Materials Task Reviews, NASA Langley Research Center, Hampton, VA, April, 1995.

16. J.K. Donald and J. Ruschau, "Direct Current Potential Difference Fatigue Crack Measurement Techniques", in Fatigue Crack Measurements: Techniques and Applications, K.J. Marsh, R.O. Ritchie and R.A. Smith, eds., EMAS, West Midlands, UK, p. 11, 1991.

17. NASA-UVA Light Aerospace Alloy and Structures Technology Program, SEAS Report No. UVA/528266/MSE96/119, University of Virginia, Charlottesville, VA, January, 1996.

18. NASA-UVA Light Aerospace Alloy and Structures Technology Program, SEAS Report No. UVA/528266/MS96/120, University of Virginia, Charlottesville, VA, June, 1996.

(a)

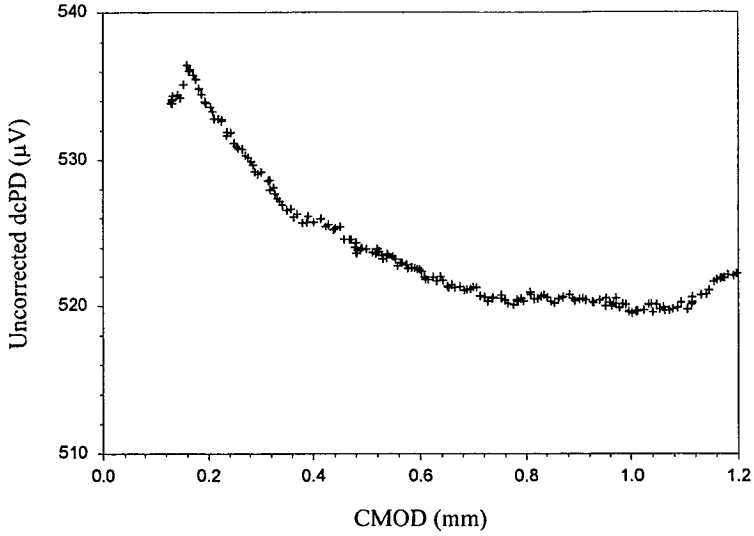

(b)

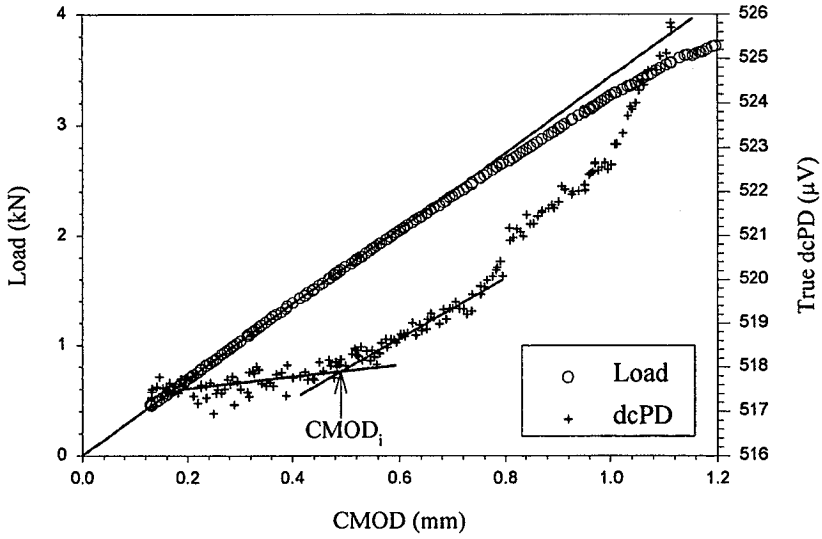

(c)

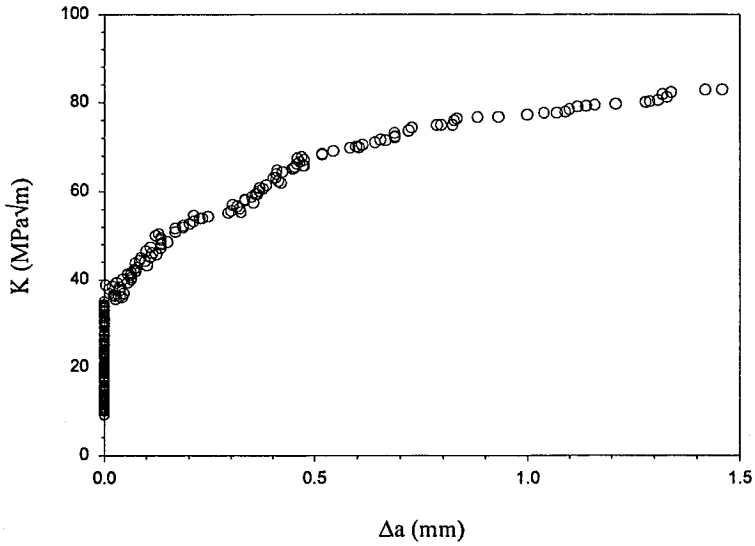

Figure 1 Evolution of data from replicate rising CMOD R-curve test for sheet 17.

(a)

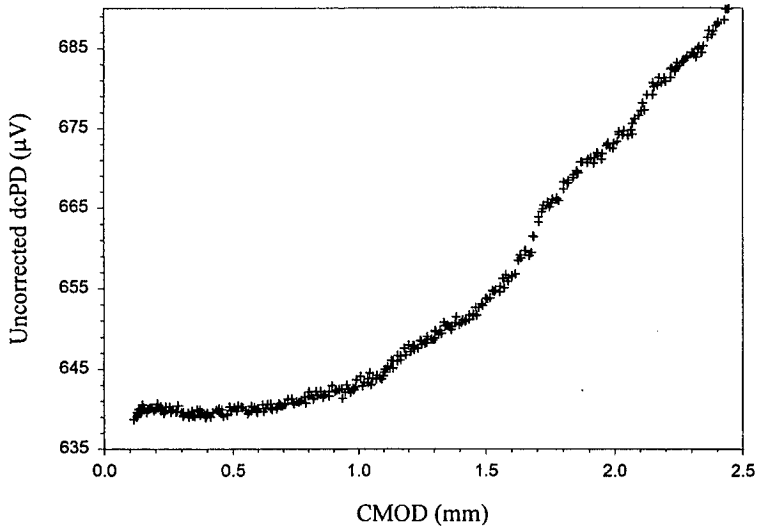

(a)

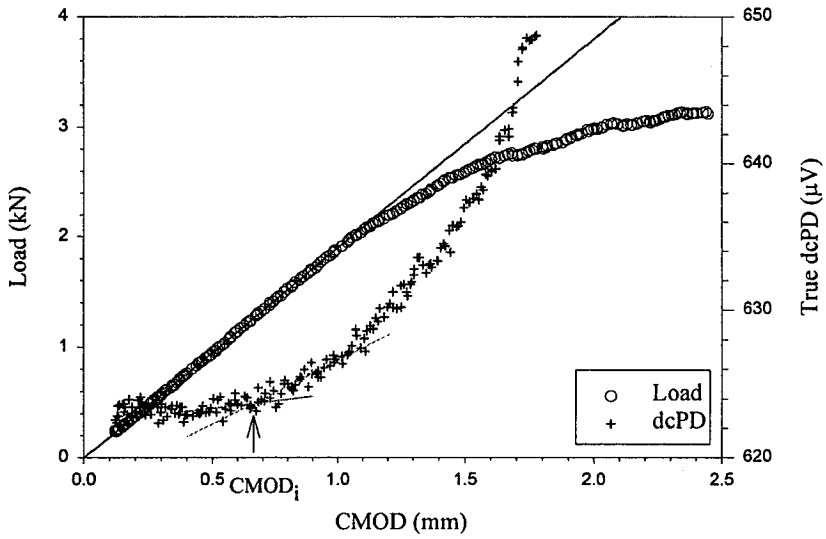

(a)

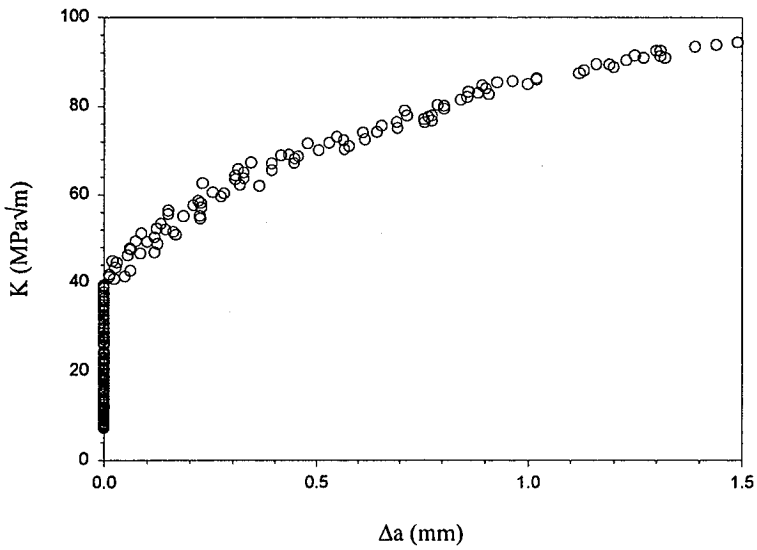

Figure 2 Evolution of data from replicate rising CMOD R-curve test for sheet 18.

(a)

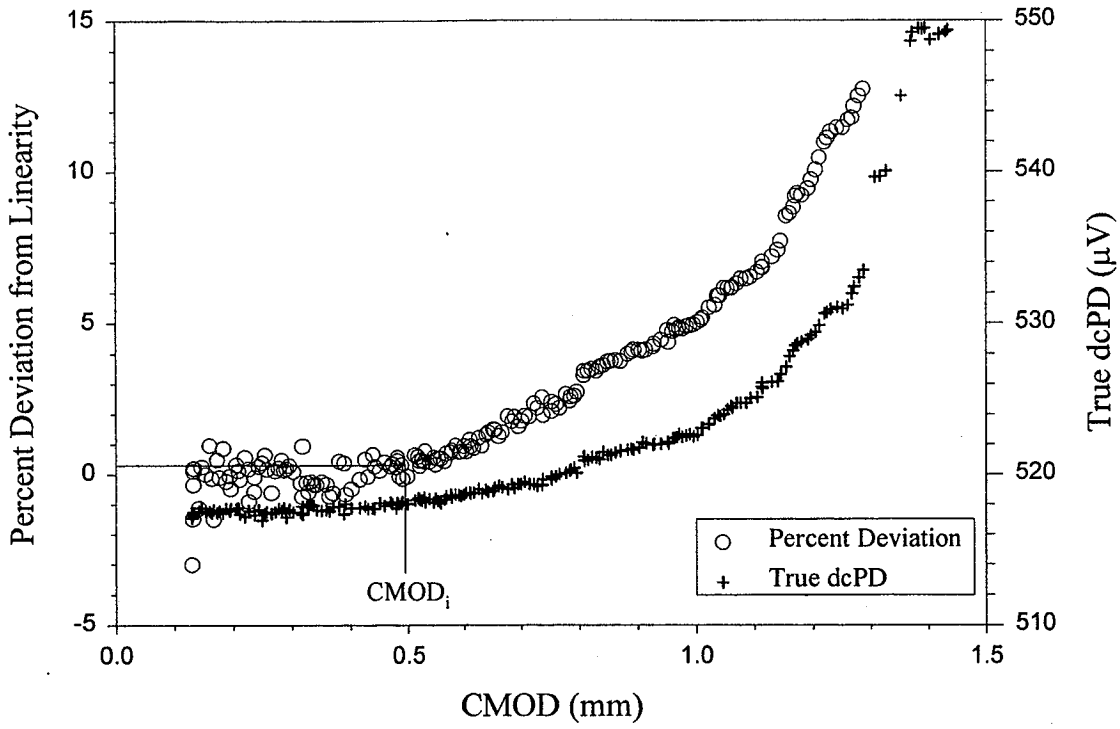

(b)

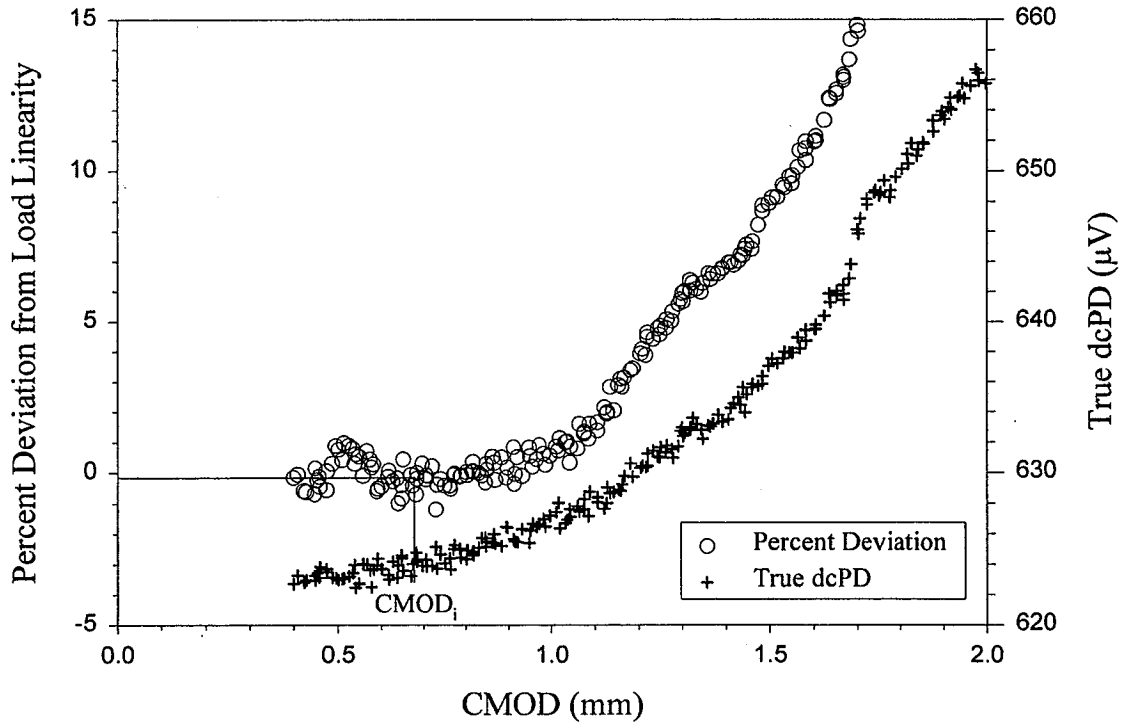

Figure 3 Percent deviation from load vs CMOD linearity and true sample dcPD vs CMOD for sheet 17 (a), and sheet 18 (b). The crack mouth opening displacement at dcPD-detected initiation ($CMOD_i$) is labelled and the corresponding percent deviation from load linearity is marked.

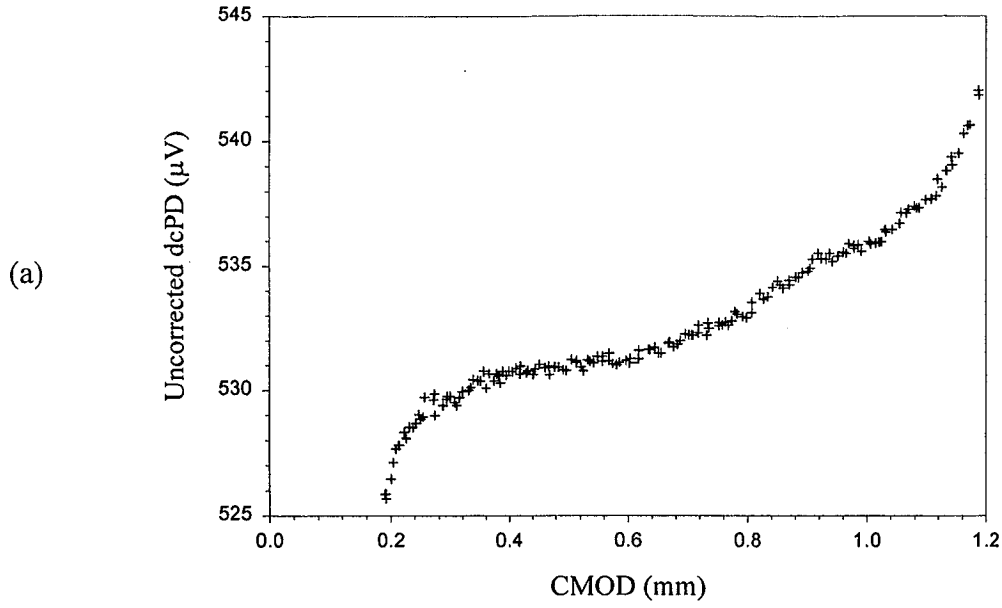

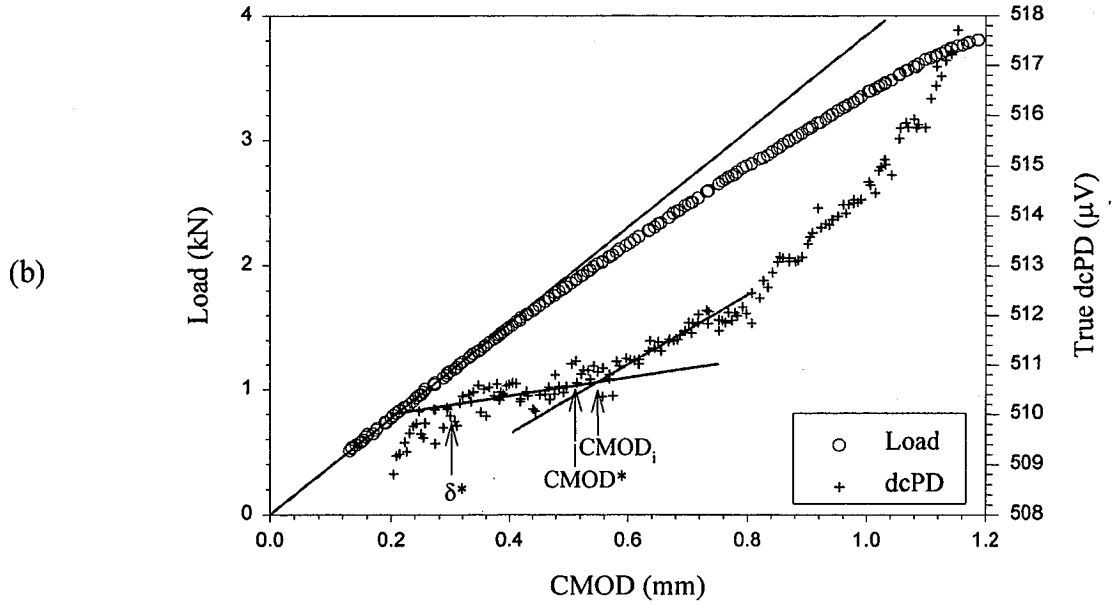

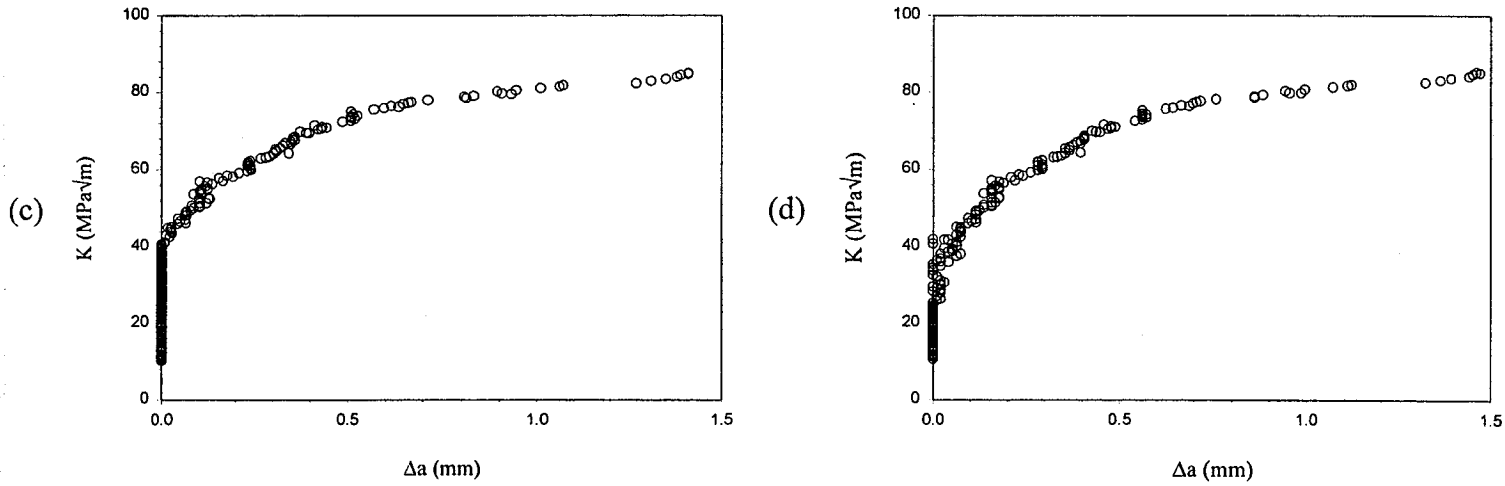

Figure 4 Evolution of data from replicate rising CMOD R-curve test for sheet 16. The R-curve in (c) is based on dcPD-detected initiation while initiation in (d) is based on non-linearity in load vs CMOD.

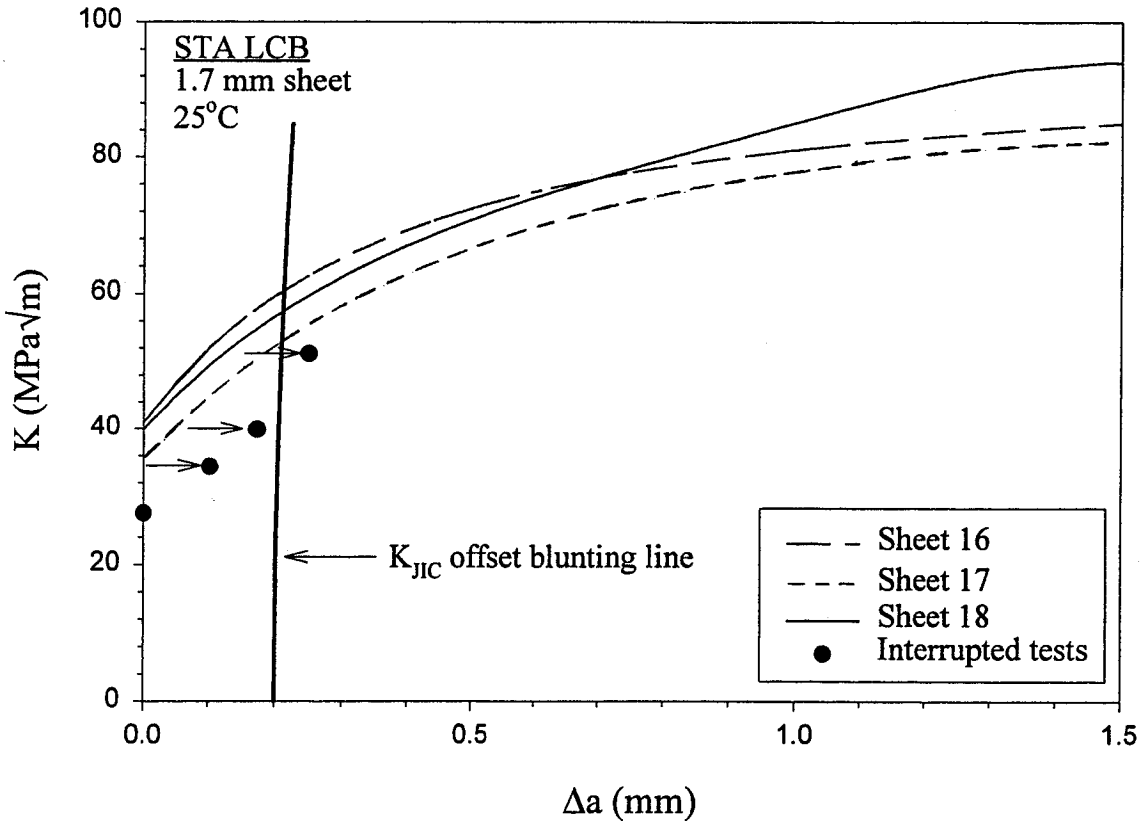

Figure 5 K vs Δa for LCB sheet specimens (Sheets 16, 17, and 18) and data from interrupted rising CMOD tests at room temperature.

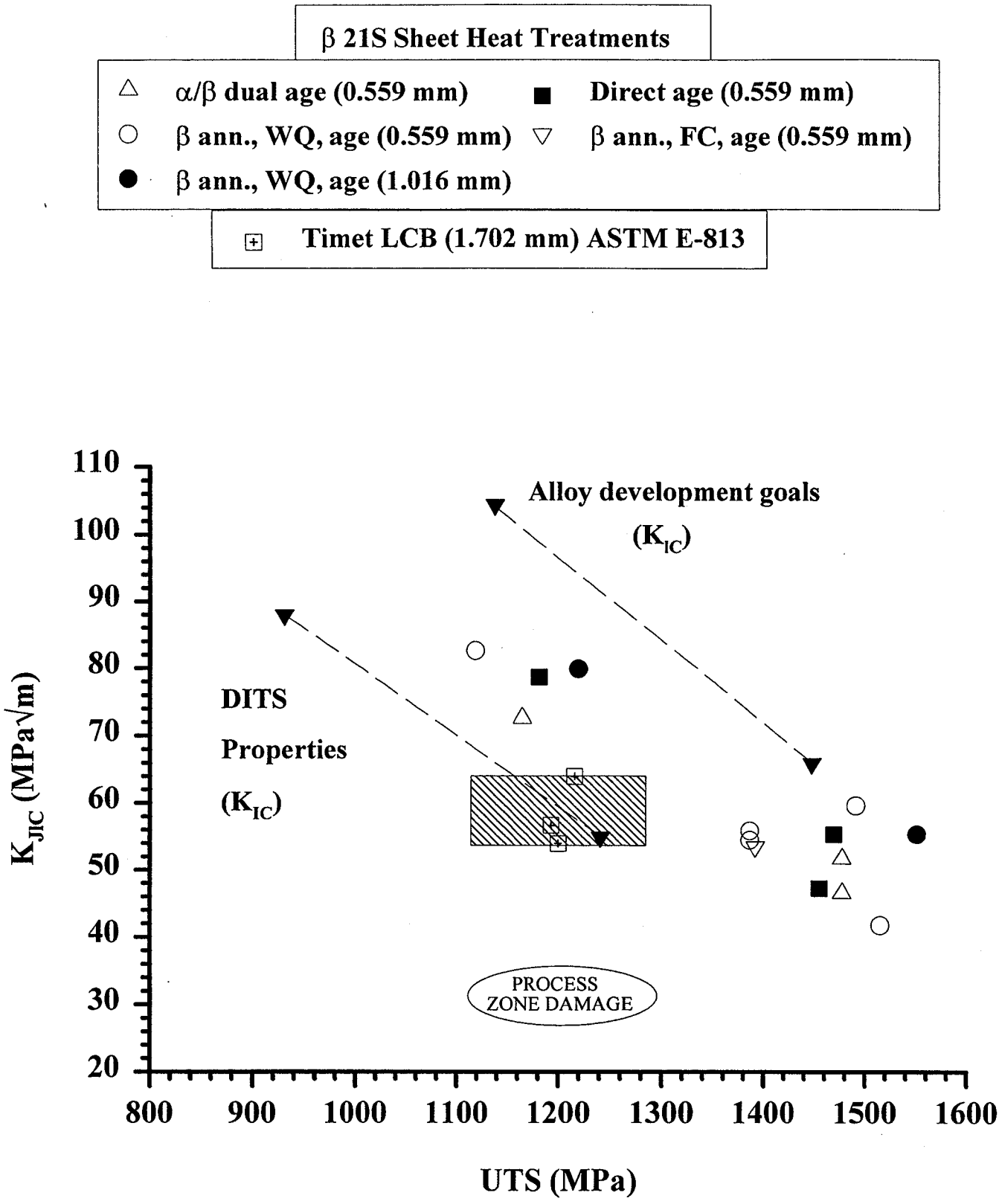

Figure 6 Initiation fracture toughness (K_{JIC}) versus ultimate tensile strength for STA LCB sheet and Beta-21S processed in different ways.

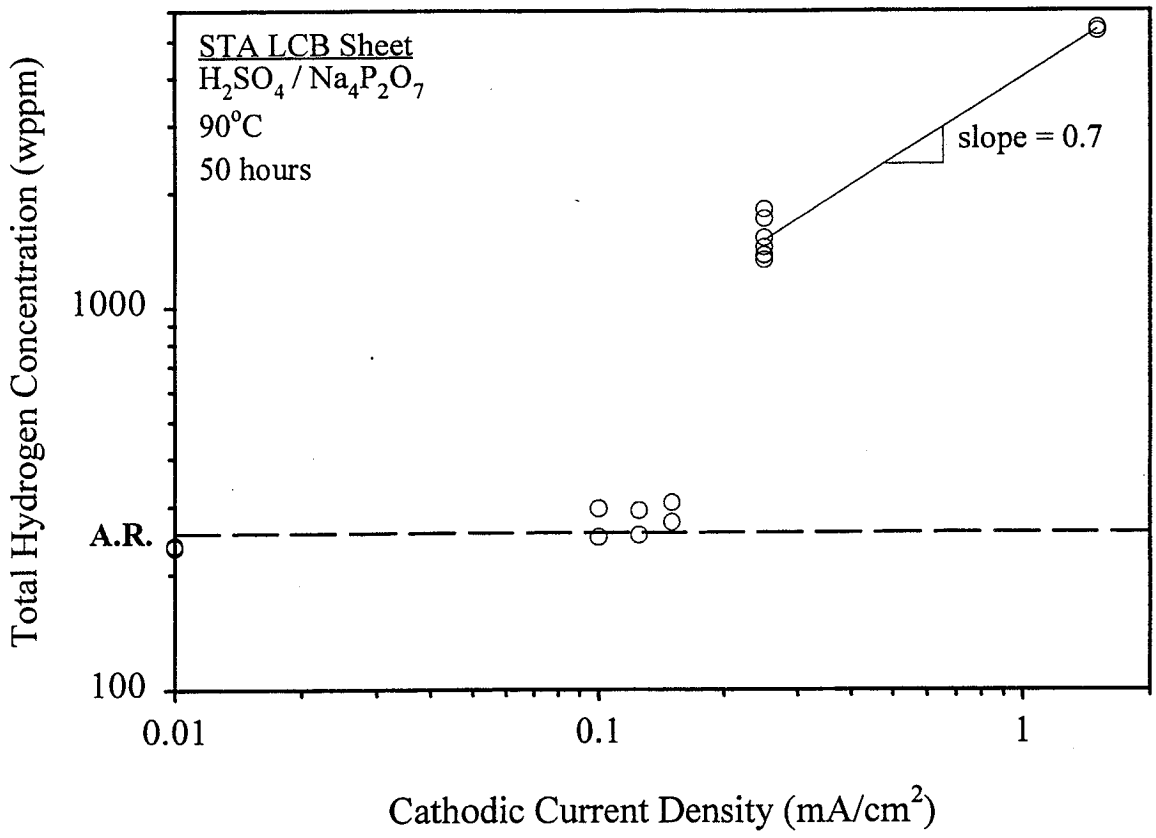

Figure 7 Calibration relationship of total dissolved hydrogen concentration versus cathodic current density on log-log axes for surface treated STA LCB sheet.

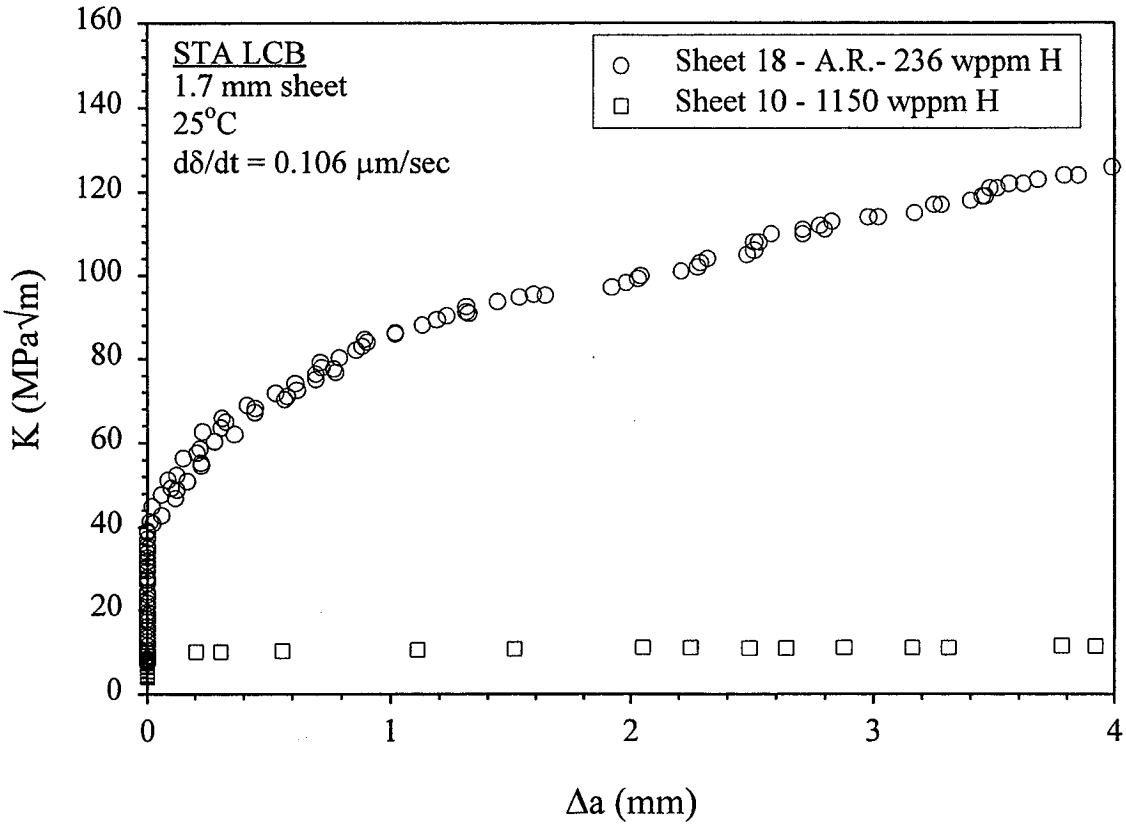

Figure 8 K vs Δa for LCB sheet CT specimens with different dissolved hydrogen concentrations.

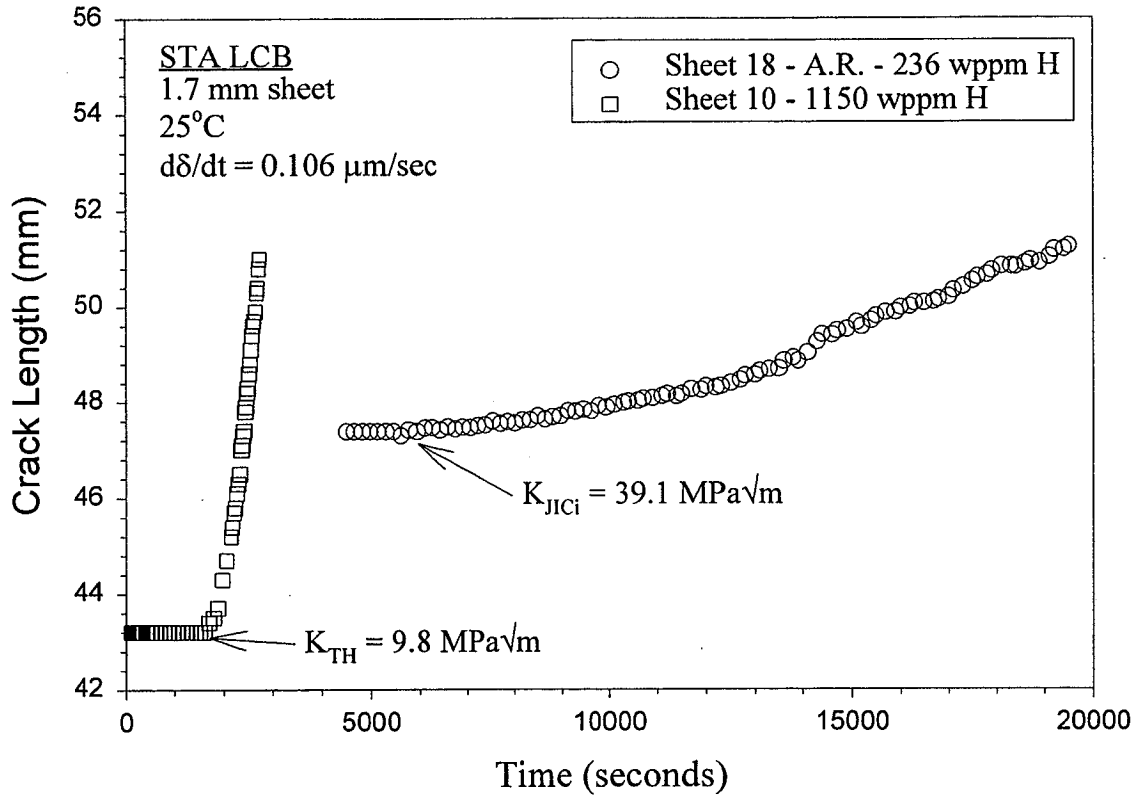

Figure 9 Crack length vs time for LCB sheet CT specimens with different dissolved hydrogen concentrations. The corresponding K-Δa curves are shown in Figure 8.

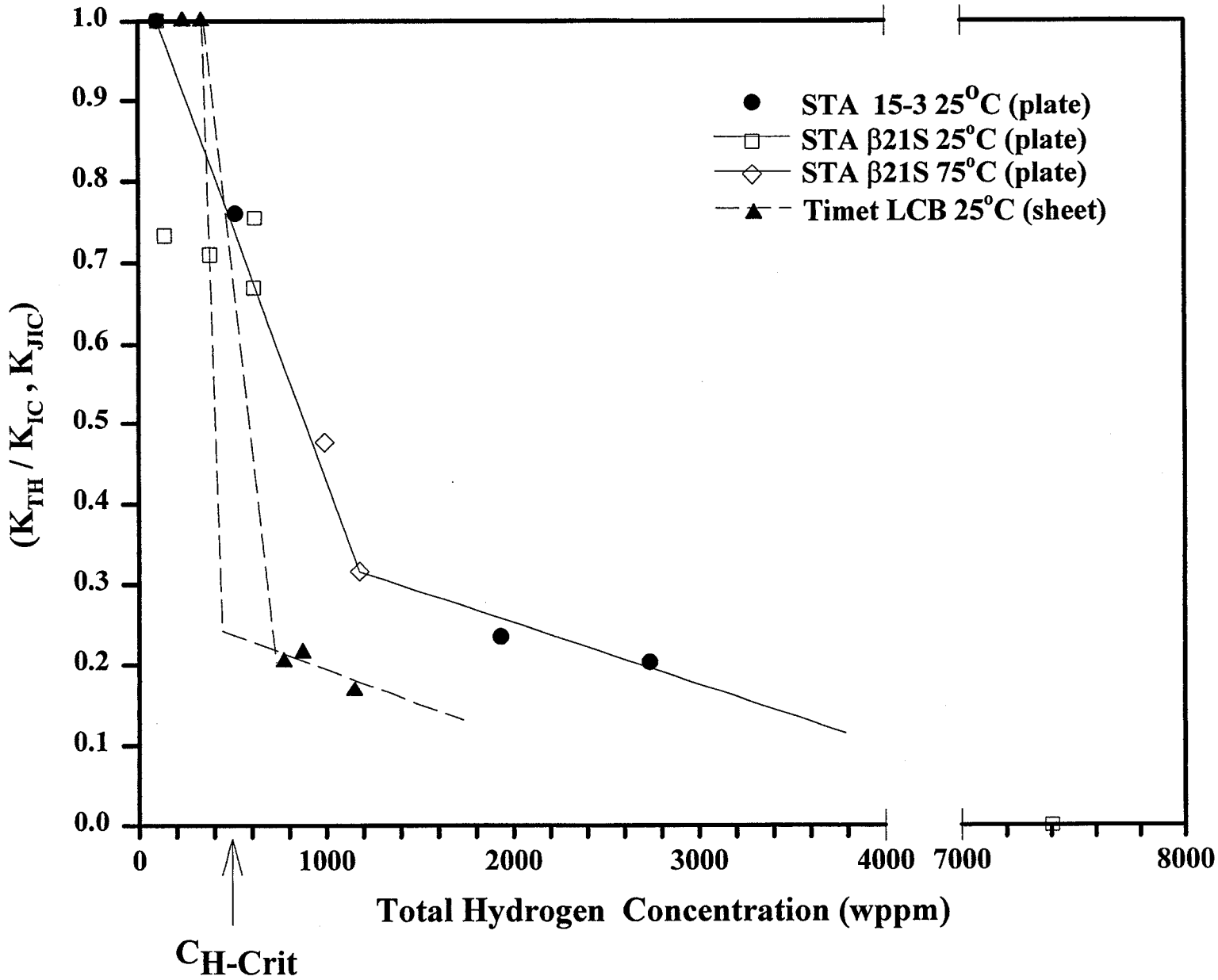

Figure 10 Ratio of threshold stress intensity for hydrogen cracking to initiation fracture toughness in air versus total hydrogen concentration for STA β-Ti alloys fractured by slow loading.

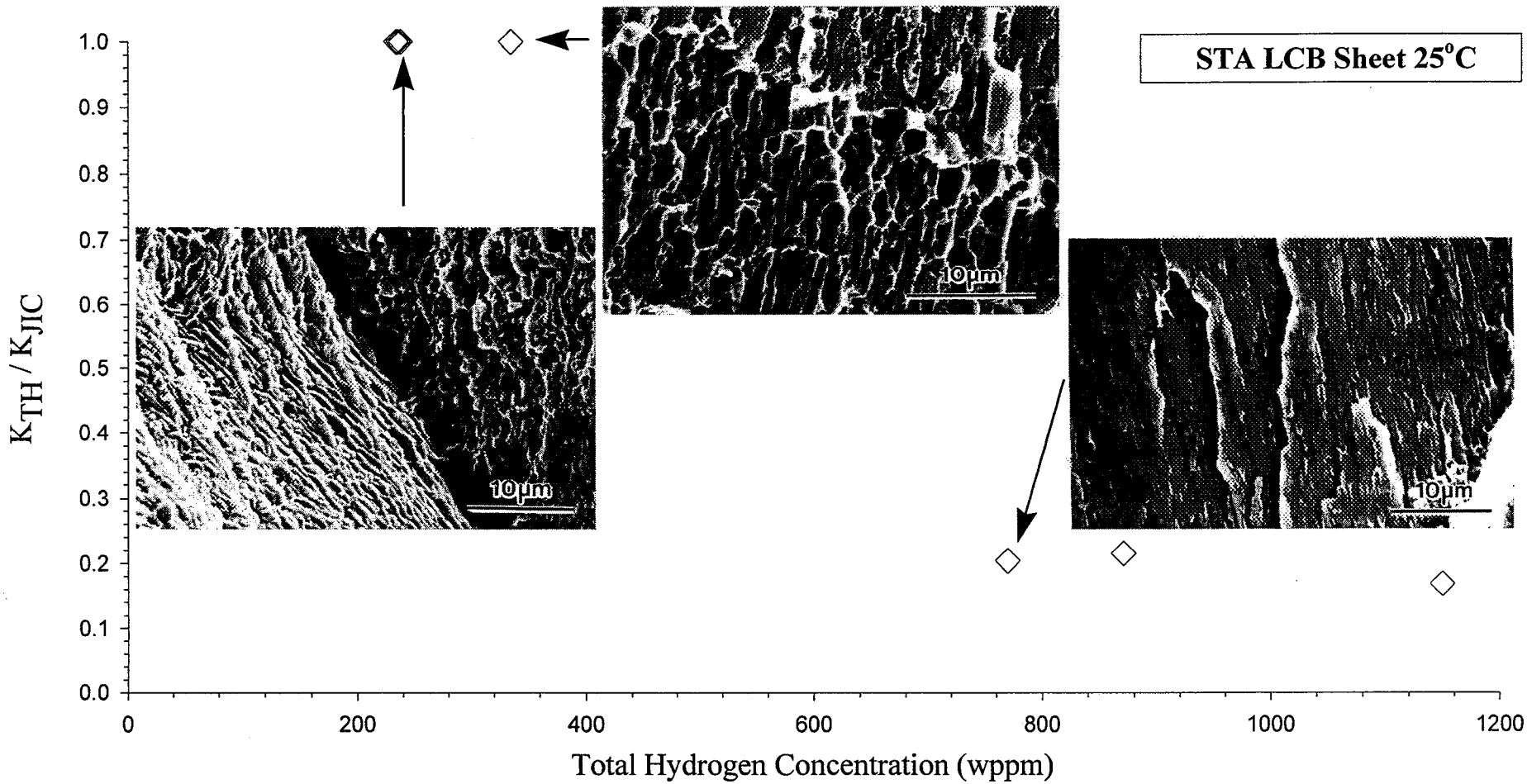

Figure 11 Ratio of threshold stress intensity for hydrogen cracking to initiation fracture toughness in air versus total hydrogen concentration for STA LCB sheet. Fracture mode changes from dimpled rupture to transgranular failure with increasing hydrogen concentration.

Project 2: Mechanisms of Deformation and Fracture in High-Strength Titanium Alloys: Effects of Temperature and Microstructure

Susan M. Kazanjian, Hinrich Hargarter, and Edgar A. Starke, Jr.

Research Objectives

The aim of this project is to identify the mechanisms by which damage occurs in β-titanium alloys, and their dependence on microstructural variations and temperature. The effects of the following factors which can influence fracture mechanisms will be investigated:

i. grain size of the beta phase,
ii. alpha volume fraction,
iii. grain boundary alpha formation,
iv. the presence of metastable phases,
v. alpha morphology,
vi. crystallographic texture and
vii. temperature at which deformation takes place.

Microstructures and textures will be altered by varying thermomechanical processing sequences so that mechanical properties and deformation modes can be determined for various metallographic conditions.

Background and Approach

Although the material of primary interest in this program had been TIMETAL LCB (Low Cost Beta: Ti-6.8Mo-4.5Fe-1.5Al), for many reasons, including unavailability of material and waning interest of NASA, investigative efforts are now focused on a slightly lower strength, higher fracture toughness β alloy, TIMETAL 15-3 (Ti-15V-3Cr-3Sn-3Al). Currently slated for use in the form of 0.0055 inch foil face sheets for the TIGER laminate system, Ti-15-3 has been recognized as possessing inadequate fatigue resistance for this application. Understanding mechanisms of deformation in this alloy will increase the possibility that processing can be designed to produce microstructures which will improve fatigue performance with minimum sacrifice of strength, ductility and fracture toughness, optimizing the balance of mechanical properties.

properties.

After initial characterization of as-received material, several thermomechanical (T/M) heat treatments will be performed to produce the various microstructures described in Table I. These material conditions were chosen, not only because they are new and improve some property of the material over standard solution treatment (ST) and aging, but also because of the variation in microstructural features they generate. We will be able to consider the effects of inhomogeneity of size and distribution of lathe α precipitated from recrystallized and from worked structures. During this work we will pay attention to effects of grain size and shape as well as the variation strength levels achieved from the different processes.

Standard solution treatment in the β phase field, above 770°C for Ti 15-3, followed by aging results in a distribution of acicular α phase in a β matrix. For this project, all materials will be solution treated at 800°C. The duplex (high/low temperature) aging process was developed to improve the fracture toughness/strength balance of this alloy by creating a tortuous crack path through a bimodal structure of coarse and fine α precipitates.[1] The intended result of triplex aging is a more homogeneous distribution of the coarse α than that developed during duplex aging. This was not found to be beneficial to fracture toughness or strength [1], but may have a significant effect on fatigue resistance. Cold rolling after solution treatment results in directional formation of α precipitates during the aging process. [2] When cold work exceeds 50% prior to aging, α predominantly precipitates at subgrain boundary nodes within the worked β structure.[3] No condition combining cold work with duplex aging will be examined since researchers have already discovered that the high/low aging process reduces the effect that cold work has on precipitation during aging.[4] Cross-slip and secondary slip activated during warm rolling prior to aging result in an aged structure with a fairly non-directional, uniform distribution of finer α precipitates.[2]

Measurements of baseline texture, tensile strength, ductility, fracture toughness, fatigue initiation resistance and fatigue crack growth resistance will be performed on all T/M variants produced. Examination of the deformed microstructure compared to the as-processed microstructure will be conducted in a transmission electron microscope (TEM) to identify the nature of deformation taking place. Fracture surfaces will also be evaluated using a scanning electron microscope (SEM).

This research will be conducted in cooperation with Professor Henry Rack of Clemson

University whose students have been studying phase transformations in β-titanium alloys. [5] Since α phase morphology in these alloys is sensitive to small changes in temperature within the α + β phase field, strict control of the relatively high temperatures required for rolling titanium must be maintained during rolling. For this reason, the rolling will most likely be conducted at a research lab such as G.E. Schenectady, NY.

Progress During the Reporting Period

Since the thickness of the Ti-15-3 foil used in the TiGr application is not conducive to fatigue testing in conventional specimen configurations, thicker sheet material will be used to determine mechanical property dependence on microstructure and texture. However, the condition of the foil as Boeing receives it from TIMET remains of interest as it determines what property advantages might be gained from subsequent heat treatment procedures. Immediately upon receipt of the foil, it was examined to detect the presence of any alpha case. This alloy is particularly susceptible to oxygen penetration of the surface during solution treatment and aging in an unprotected atmosphere. This oxygen facilitates transformation to alpha phase of the infiltrated surface layer upon cooling. Such an alpha case would adversely affect fatigue properties. However, no case was visible upon optical or SEM inspection, Figure 1.

After the as-received microstructure of the foil was identified as 100% beta by x-ray diffractometry, Figure 2, texture measurements were made to determine the degree to which cold rolling this material crystallographically reoriented the grains. Individual pole figures measured for the (110), (200) and (211) poles are presented in Figure 3. The ODF generated from these poles is shown in Figure 4. For the great amount of cold rolling this foil received, texture analysis shows surprising little preferred orientation.

Specimens of the 0.0055 inch foil were solution treated, quenched, then aged at a variety of temperatures to determine the aging response of the material currently in service. These specimens were encapsulated in argon filled quartz tubes to prevent oxygen pick-up. Two different solution treatment temperatures were used prior to aging in order to distinguish the effect of grain growth and vacancy concentration on α morphology in the foil. Beta solution treatment of 0.0055 inch foil at 843°C for times ranging from 5 to 60 minutes revealed that recrystallization of this heavily deformed microstructure occurs quickly, allowing growth to commence. There is significant grain size variation between specimens solution treated for 10, 30 and 60 minutes, as

evident in Figure 5. Evaluation of specimens β solution treated at 788°C and 843°C for 5, 10, 30 and 60 minutes; and specimens subsequently aged for 8 hours at 483°C and 538°C will produce a catalog of microstructural possibilities for the foil material. Alpha morphology appears very uniform in all of the aged samples already examined. An example is shown in Figure 6. This comparison of microstructures is continuing.

Initial microstructural, crystallographic and mechanical property evaluation of 0.090 inch thick TIMETAL Ti-15-3 sheet received in September has begun. X-ray diffractometry revealed that this material is also 100% beta phase, Figure 7. Little crystallographic texture is distinguishable from the pole figures recorded from (110), (200) and (211) poles, Figure 8, and their corresponding ODF, Figure 9. However, tensile tests did reveal some anisotropy of properties. Yield strength varied from 739 MPa measured parallel to the rolling direction to 766 MPa measured in the transverse direction. Results listed in Table II are averaged from duplicate tests. These low strength values prompted us to forego fatigue testing of as-received materials and begin heat treatment of specimens.

Heat treatment facilities have been assembled that allow solution treatment and aging of tantalum wrapped specimens of Ti 15-3 in a slowly flowing argon atmosphere. This atmosphere control is required to prevent oxygen gettering and subsequent α case formation on the specimens during heat treatment. Specimens have already been prepared in the solution treated-standard aged form.

Fatigue initiation will be measured by recording cycles to achieve 0.005 inch crack extension from the center hole of a middle crack tension specimen of geometry shown in Figure 10a. A slight grip modification is underway. When complete, fatigue initiation testing will begin. Fatigue crack growth testing will proceed on specimens of the extended compact tension design shown in Figure 10b. The direct current potential drop (DCPD) method will be used to measure crack extension. Fracture Technology Associates, Inc. (FTA), software will be employed to measure and report da/dN as a function of ΔK. Tensile and fracture toughness tests will also be performed on representative samples from each T/M variety produced.

Conclusions

Work on the development of microstructures and mechanical properties of TIMETAL LCB has been suspended for this portion of the project.

Inspection of the foil as supplied to Boeing showed no presence of α case which could deteriorate fatigue performance.

In the as-received, cold-rolled, 100% β condition, neither 0.0055 inch nor 0.090 inch thick material exhibit significant crystallographic texture.

Aging of the 0.0055 inch thick foil can produce a variety of alpha morphologies that should change fatigue performance in service. However, we have not developed a satisfactory method of determining fatigue performance of thin foil in the laboratory.

Tasks for the Next Reporting Period

The main thrust of this project during the next few months will be recognition of deformation taking place during fatigue and tensile testing. Fatigue testing of 0.090 inch thick sheet in various heat treated conditions is underway. Microscopic examination of deformed specimens will begin when tested specimens are available. Observation of material tested in the β-solution heat treated and quenched condition may be required to reduce the complexity of the microstructure and provide information on deformation in the beta phase. After this is determined, deformation in the more complex aged structures may be more easily discernible.

References

1. Naotake Niwa and Hideo Takatori, "Effect of Step-Aging on the Fracture Toughness of Ti-15V-3Cr-3Sn-3Al Alloy", *Beta Titanium Alloys in the 1990's,* ed. D. Eylon, R. Boyer, and D. Koss, TMS, 1993, 237-247.

2. H. Ohyama, Y. Ashida, T. Nishimura, T. Maki, "Effects of Temperature on Deformed and Aged Microstructures and Tensile Properties in Ti-15V-3Cr-3Sn-3Al", *ISIJ International.,* v 33 (1993), no. 8, 889-897.

3. Teruhiko Inaba, Kei Ameyama and Msaharu Tokizane, "Formation of (α + β) Microduplex Structure in A Ti-15V-3Cr-3Sn-3Al Alloy", *ISIJ International*, v 31 (1991), no. 8, 792-798.

4. Naotake Niwa, Akira Arai, Hideo Takatori and Kunio Ito, "Mechanical Properties of Cold-Worked and High-Low Temperature Duplex Aged Ti-15V-3Cr-3Sn-3Al Alloy", ISIJ (1991), 856-862.

5. Sébastien Azimzadeh, "Phase Transformations in Metastable β Titanium Alloys," Master of Science Thesis, Clemson University, December, 1995.

Table I. Proposed Thermo-Mechanical Treatments.

Condition	Aging Temp/time (°C) / (hrs)	Resulting Microstructure	Tensile Properties		Benefits
	T1/t1		UTS (MPa)	% Elong	
Solution Treated	-	Entirely beta	780	23	
Standard Age	540 / 8	Lathe alpha ppt on g.b.'s and within β grains. PFZ's along g.b.'s	1000	14	
Duplex Age	600 / 14 to 28 400 / 50 to 100	Bimodal distribution of coarse and fine α ppt within β grains			Enhances fracture toughness by creating tortuous crack path.
Triplex Age	300 / 10 600 / 3 to 6 450 / 100	Homogeneously distributed coarse α ppt prior to high-low aging			Reduces benefit of duplex age on fract. toughness, presumably due to increased homogeneity of microstructure.
60%CR + Age	540 / 8	Lathe shaped α within β grains. Reduces g.b. ppt of α by providing dislocations as homogeneously distributed nucleation sites.	1200	10	Increases strength without loss of ductility. Increases rate of strengthening, reducing required aging times.
60% WR at 600°C+ Age	540 / 8				

Table II: Timetal 15-3 Tensile Properties

Specimen	No. of Tests	Yield, 0.2% ksi [MPa]	UTS ksi [MPa]	Fracture Stress ksi [MPa]	Elongation (%)
Foil, RD	2	107 [739]	107 [739]	72 [493]	36.1
Foil, TD	2	111 [766]	111 [766]	67 [460]	22.3

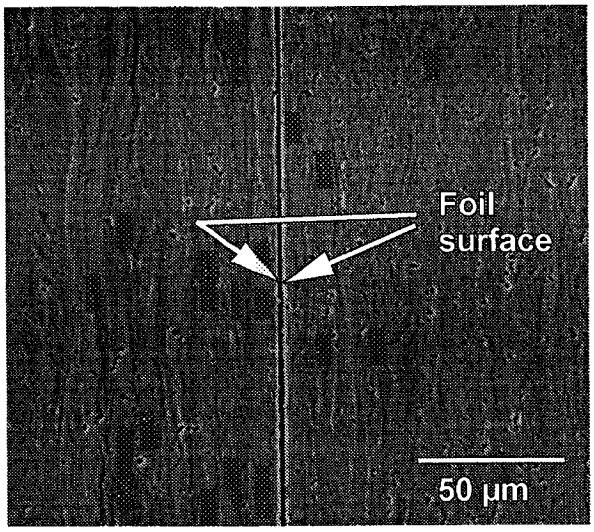

Figure 1. Cross-section of foil exhibiting no evidence of α case.

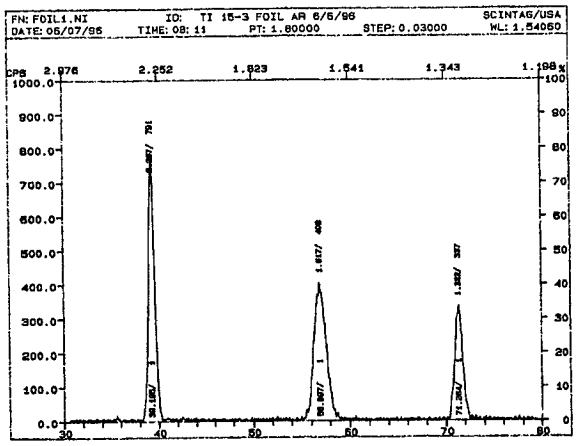

Figure 2. X-ray diffraction of the foil exposed only those peaks characteristic of the beta phase.

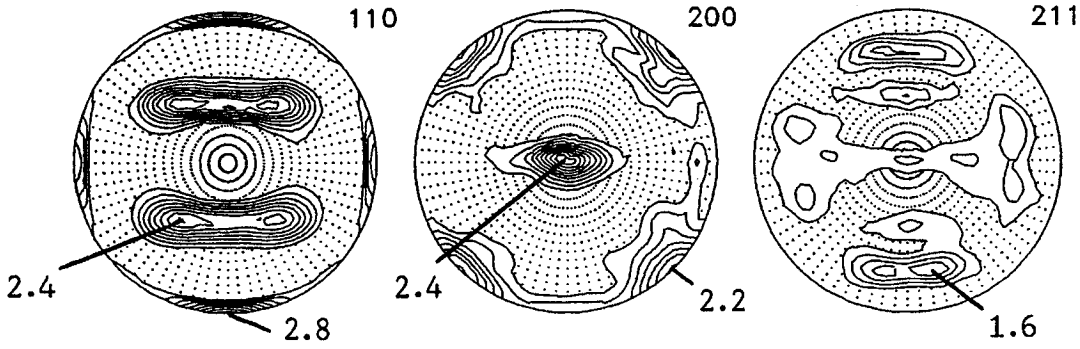

Figure 3. Individual $\{110\}_{beta}$, $\{200\}_{beta}$ and $\{211\}_{beta}$ pole figures measured on as-received 0.005 inch foil.

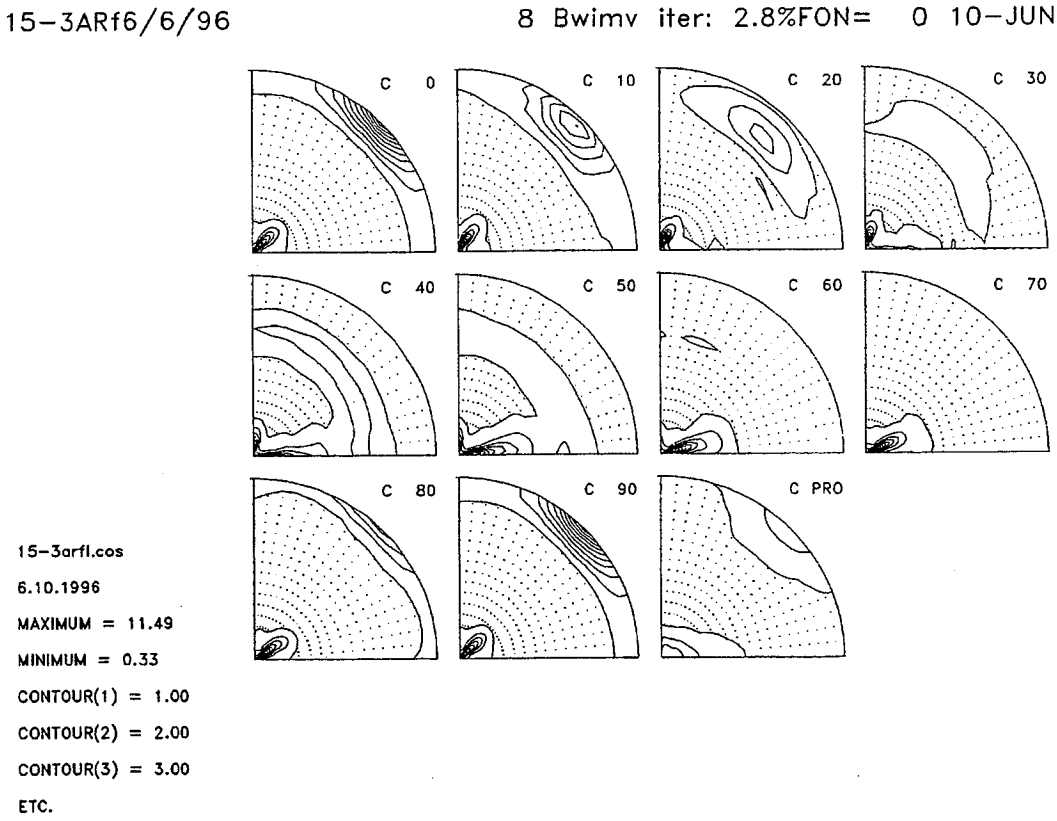

Figure 4. Orientation Distribution Function (ODF) calculated for as-received 0.0055 inch foil from pole figures above.

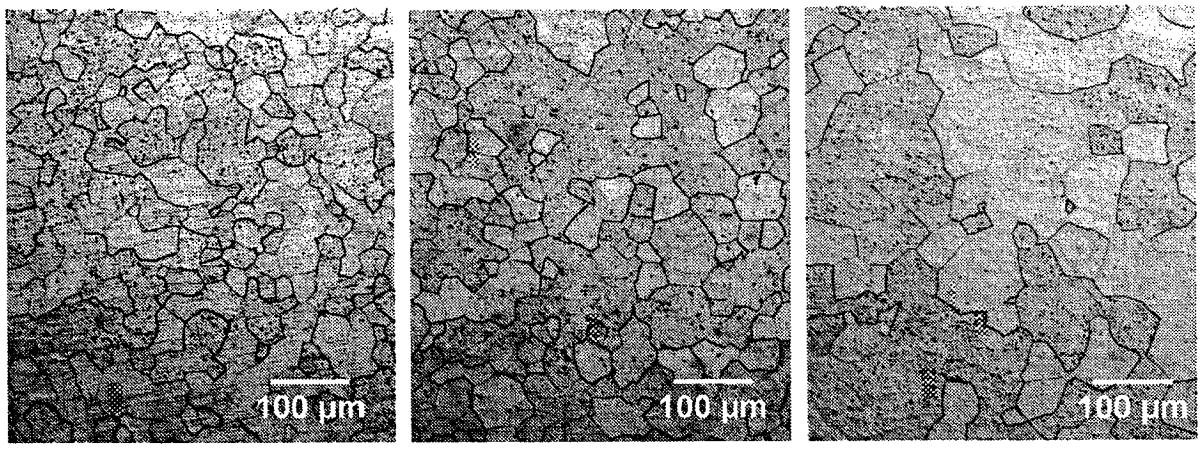

(a) (b) (c)

Figure 5. Grain growth occurring during beta solution treatment at 843°C for (a) 10 minutes, (b) 30 minutes and (c) 60 minutes.

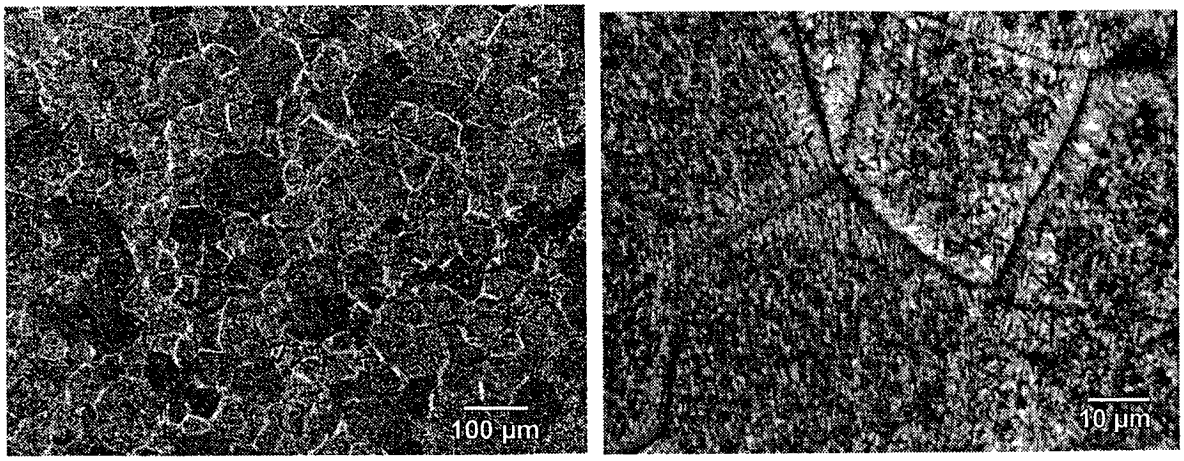

Figure 6. Foil solution treated at 843°C for 30 minutes, then aged for 8 hours at 538°C.

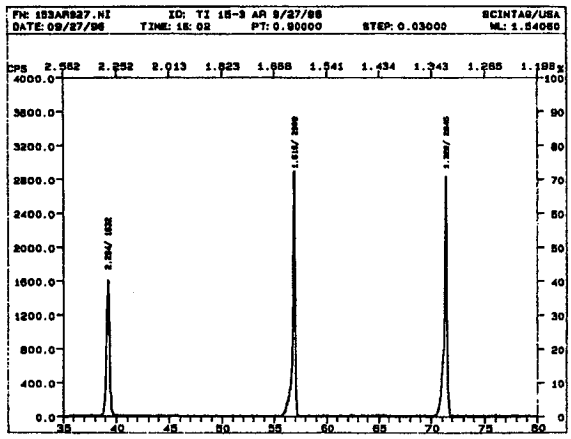

Figure 7. X-ray diffraction of the sheet exposed only those peaks characteristic of the beta phase.

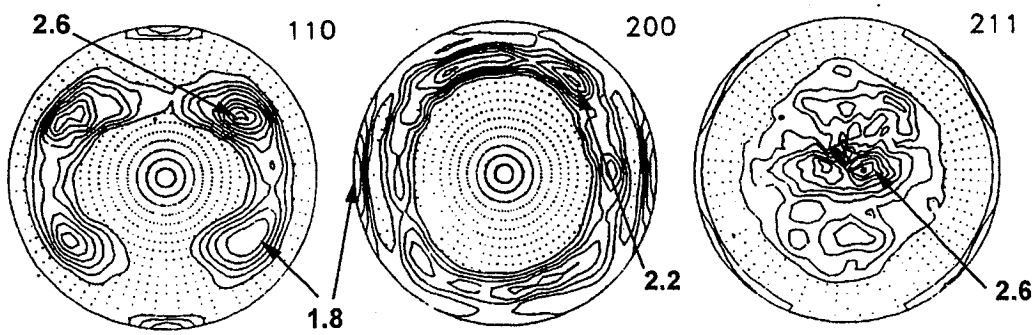

Figure 8. Individual $\{110\}_{beta}$, $\{200\}_{beta}$ and $\{211\}_{beta}$ pole figures measured on the 0.090 inch sheet in the as-received condition.

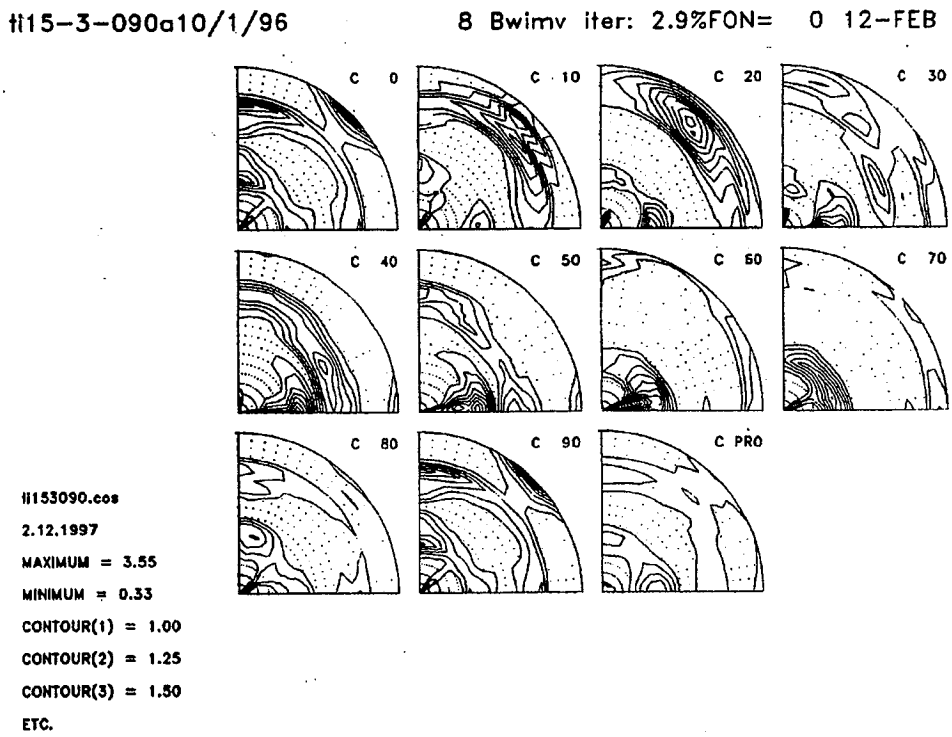

Figure 9. ODF generated for as-received 0.090 inch sheet.

Note: Dimensions in inches.

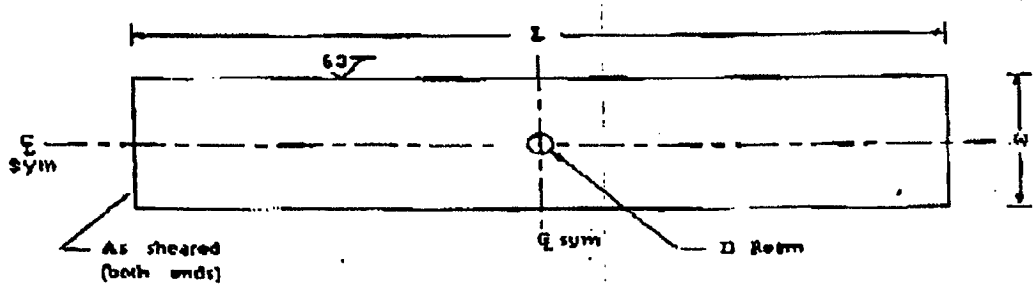

(a)

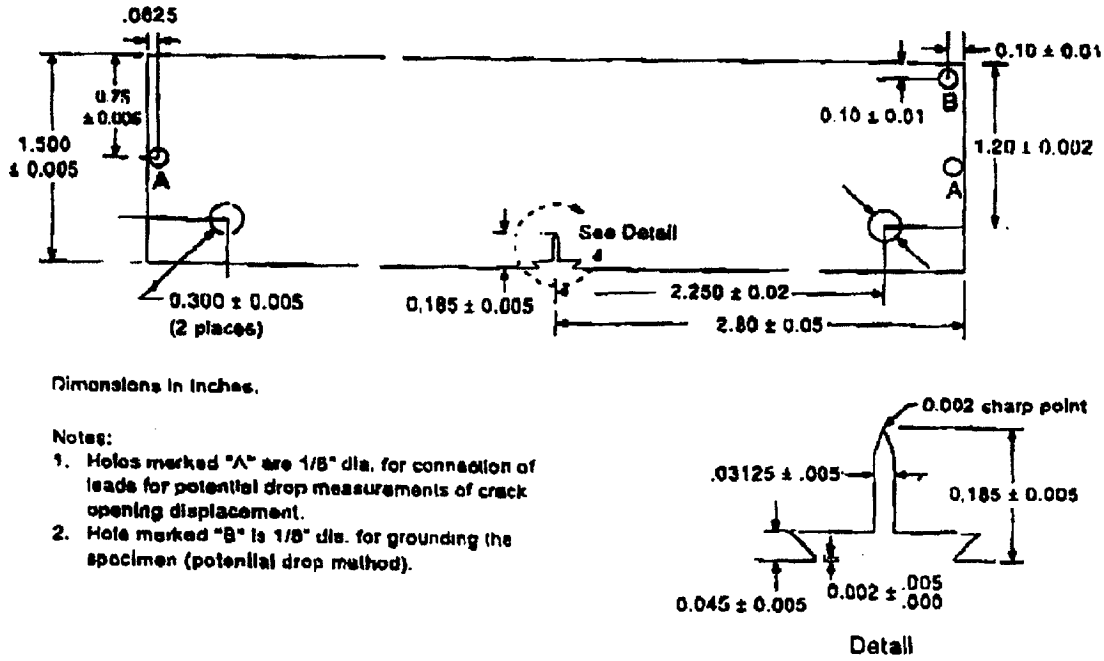

(b)

Figure 10. Specimens to be used in the fatigue portion of this investigation,(a) fatigue crack initiation, (b) fatigue crack growth.

Project 3: Effect of Texture and Precipitates on Mechanical Property Anisotropy of Al-Cu-Mg-X and Al-Cu alloys

Hinrich Hargarter, and Edgar A. Starke, Jr.

Research Objectives

It is the objective of this project to determine the combined effects of texture and plate shaped precipitates on the yield stress anisotropy in aluminum alloys. The influence of externally applied elastic stresses during aging on the precipitation shall be investigated in view of its implications on the applicability of the Age Forming manufacturing technique. Based on the experimental observations, a theoretical model shall be developed which is capable of quantitatively or qualitatively predicting anisotropy in wrought aluminum products. During the reporting period the investigations focused on the influence of elastic stresses on the precipitation of Θ' and the resulting influence on yield stress anisotropy.

Background and Approach

Anisotropic behavior , i.e. the resistance to yielding with respect to the direction of loading, is normally attributed to the crystallographic texture. The analysis of Taylor [1] and Bishop and Hill [2] provides a theoretical basis for the prediction of anisotropy in a single-phase polycrystalline FCC metal or alloy. Many age hardenable aluminum alloys contain plate shaped precipitates having specific crystallographic habit planes, e.g. {100} for Θ' and {111} for Ω and T_1. These phases should result in changes in the plastic anisotropy. Indeed, it was observed, that precipitates on {100} will act to reduce texture-induced anisotropy while those on {111} enhance texture effects. Hosford et al. [3] and Bate et. al. [4] developed theoretical models to explain the effect of precipitates on plastic anisotropy in aluminum alloys.

An earlier result of this project was that the application of elastic stresses during aging of Al-Cu-Mg-Ag-alloys caused preferential precipitation of Θ' and Ω on favorably oriented variants of their habit planes [5]. Without stress, an equal number of Θ' precipitates should form on all three {100}-variants and on all four variants of {111} for Ω respectively. Under the influence of an externally applied elastic tensile stress, higher number densities of both phases were found on those habit planes that formed the smallest angle with the load. It was also observed that the main

influence was on precipitate nucleation, and that a certain critical stress had to be exceeded to obtain preferential precipitation . Θ' required approximately 20 MPa, whereas the critical stress for Ω was 120 MPa. These findings can be explained by the critical role of the precipitate misfit on nucleation. Precipitates which have a negative misfit with the matrix due to volume and shape differences should nucleate preferentially parallel to a tensile stress field.

It is clear that Stress Aging, i.e. the external application of stresses during aging, should result in a change of anisotropy. Not only because of its influence on average number density, volume fraction and dimensions, but also because of the changes in the geometrical arrangement of the precipitates. Different effects can be anticipated for Θ' and Ω. Further important factors that should also contribute to changes in the anisotropy and therefore need to be taken into account include: The way dislocations interact with a particular strengthening precipitate, i.e. whether the particles are sheared by dislocations or not, and possible interactions when several different precipitate phases are present.

The objective was approached by stress aging of sheet under applied tensile loads and subsequent preparation of tensile specimens parallel, perpendicular and 45° to the load axis. The measured yield stress anisotropy reflects the combined influences of stress-induced precipitate alignment and of the crystallographic texture. Tensile tests were also performed in the same orientations on as-quenched and conventionally aged material. The former reflect only texture-induced anisotropy and the latter allows to differentiate between the effects of randomly distributed and preferentially aligned precipitates.

A creep frame was redesigned to allow the attachment of a temperature chamber, which ensured a homogenous aging temperature over a much larger area than the conventionally used furnace. Rectangular specimens with approximate dimensions of 250 x 60 x 3 mm were prepared parallel to the rolling direction of sheet material, solutionized, water quenched and subsequently aged. It is important to note that the load was applied before the furnace was turned on. The crystallographic texture of the sheet was determined at half thickness using a Siemens X-ray texture goniometer with Cu-Kα radiation. The software package POPLA was used to calculate the orientation distribution functions. Quantitative stereological measurements of the precipitate dimensions , number density and volume fraction were performed in the TEM. Data were obtained separately for each habit plane variant on images in a (100) and (110) orientation of the electron beam. Foil thickness was determined from CBED patterns. Additional microstructural

information was obtained from optical micrographs.

Initially, experimental work focused on a modified version of Al 2519 with a composition of Al-5.75Cu-0.52Mg-0.3Mn-0.49Ag-0.16Zr. This alloy contains Ω with {111} habit planes as well as Θ' on {100}. Further investigations were performed on several binary Al-Cu-alloys. These were used as a model for alloys that only form Θ'.

The theoretical prediction of anisotropy effects was approached by modifying the models developed by Hosford/Zeisloft and by Bate to explain the different influences on anisotropy of precipitates on {100} and on {111} planes. In their original form, both models presume a random distribution of the precipitates on their respective habit planes. Hosford assumed, that compatibility between the precipitates and the matrix is maintained partly by rotation and partly by plastic deformation of the precipitates [3]. The orientation dependence of strengthening by the precipitates can be represented by a parameter, N_{avg}, derived from the ratio of effective strain in the particle to that in the matrix. The analysis leads to the following expression for the flow stress in a textured material:

$$\sigma_f = M \tau (1- V_f) + V_f \sigma_p N_{avg} \qquad [1]$$

where V_f = Total volume fraction of precipitates, M = Taylor factor appropriate to the crystallographic texture, τ = basic shear stress of the matrix, σ_p = effective flow strength of the precipitates.

Bate assumed, that the change in anisotropy caused by precipitation arises solely from the orientation dependence of a long range stress (i.e. the so called back stress) caused by the precipitates [4]. His analysis gives the flow stress as:

$$\sigma_f = M \tau' (1- V_f) + 2 \mu V_f ||\gamma|| \varepsilon_p \qquad [2]$$

where $||\gamma||$ = Norm value of accommodation tensor, determined by shape and orientation of the precipitate, τ' = modified matrix shear stress, and μ and ε_p = physical constants.

Mark Lyttle has written a computer program at UVA, that allows the calculation of the predicted flow stresses for polycrystals, using the orientation distribution function as an input [6].

Progress During the Reporting Period

Two strips of the Al-Cu-Mg-Ag alloy were stress aged at 160°C for 48 hours; one under an applied tensile stress of 70 MPa the other at 140 MPa. This choice of aging parameters was based on earlier observations. Two different aging stresses were used to separate the effects of aligned Θ' from those of aligned Ω. At the lower aging stress only the precipitation of Θ' should be affected, whereas at the higher aging stress both phases should precipitate in a non-random fashion. The load axis was identical with the rolling direction of the sheet. Tensile specimens were cut from the fully heat treated strips parallel, perpendicular and at 45° to the direction of the aging stress.

Figure 1 shows the results of the yield stress measurements. Data points represent the average of two measurements and the error bars indicate the absolute difference between the two individual results. Data for the T6 condition are included for comparison.

As was mentioned before, the as quenched condition (SHT) should only reflect texture-induced anisotropy. Due to the formation of deformation zones around the large inclusions, all sheet of modified 2519 available at UVA exhibited an almost random recrystallization texture after solutionizing. Consequently, texture had only limited influence on anisotropy and the yield stress was only slightly higher at 45° than in the other directions. In the T6 and in the slightly overaged condition (48 h / 0 MPa), the combined influences of Θ' and Ω precipitation cause an opposite trend in anisotropy. The alignment of Θ' resulting from stress aging at 70 MPa produced almost isotropic yielding behavior in the sheet. A different anisotropic behavior was found when increasing the applied stress to 140 MPa. Stress induced alignment of Θ' and Ω caused the yield stress parallel and at 45 degrees to the load to follow the trend of the unstressed aging conditions whereas perpendicular to the aging stress lower yield stresses were observed.

The findings demonstrate that a redistribution of the plate shaped precipitates resulting from the application of elastic stresses during aging is indeed capable of controlling the yield stress anisotropy, although the measured anisotropy appears to be rather small. This is due to the random texture in the investigated alloy.

The crystallographic orientation of a grain with respect to the applied stress field determines the distribution of the precipitates in this grain. The probability for the nucleation of a precipitate on a specific variant of its habit plane depends on the stress field acting on this variant. If the orientation of the grain is such that the stress field is identical for all variants, the precipitate

distribution will become random again. Θ' and Ω nucleate preferentially parallel to a tensile stress. Therefore, the orienting effect will be maximized for Θ' in grains with the {100} planes parallel to the load axis, whereas Ω requires a {111} orientation. As a consequence, randomly textured material will not only show little texture induced anisotropy, but effects due to elastic stresses during aging will also be minimized.

The experimental limitations caused by the random texture and the simultaneous presence of two different precipitate phases called for a simpler microstructure. This would allow us to study the influence of stress on the precipitation of Θ' and its effects on the yield stress anisotropy in more detail. Therefore, a binary Al-Cu-alloy was requested from Reynolds Metals Company, Richmond. An Al-2.5Cu alloy was received and a processing map was developed that resulted in equiaxed grains of approximately 800 μm diameter and a cube/rotated cube recrystallization texture after solutionizing. Measurements of the age hardening response showed the desired slightly overaged condition was obtained after 48 hours @ 210°C.

However, TEM work revealed that the chosen combination of aging temperature, time and stress, did not result in the anticipated effect of significantly higher number densities of Θ' on preferentially oriented variants of {100} planes. The missing influence of the aging stress proves, preferential precipitation not only requires a critical stress, as we had observed earlier, but that certain stress/ temperature combinations are necessary.

The effect of stress/temperature combinations was studied in more depth in an Al-5Cu alloy, of which a small quantity was readily available. Tapered specimens were prepared and aged under stress using the following conditions: 24 h/ 210°C, 48 h/ 190°C, 96 h/ 175°C, 96 h/ 160°C. Tensile stresses within each specimen ranged from 20 MPa to 100 MPa. TEM specimens were prepared from the S-L plane as indicated on Fig.2a.

Figure 2b summarizes the results of the TEM investigations. Because the orientations of the grains in the TEM foils were not identical for all stress levels, results are not quantified. Instead, data are presented for the grain with the smallest angle between the stress axis and any of the two visible {100} planes on each micrograph. Preferential alignment was concluded when the number density on this variant was at least 1.5 times higher than on the other. All specimens aged at 160°C, 175°C and 190°C revealed selective precipitation of Θ' on favorably oriented habit planes at all investigated stress levels between 25 MPa and 110 MPa. In TEM foils taken from the 210°C -specimen, no grains with preferentially oriented precipitates were found. However, the

distribution of the precipitates was not identical with the truly random dispersion found in conventionally aged specimen. Instead, the precipitates were often arranged in bands, as is illustrated in Fig. 3. Although less pronounced, a similar arrangement was also found in foils taken from high stress regime of the 190°C sample. It appears likely that under the influence of the applied stress at the higher aging temperatures, nucleation of Θ' occurs primarily heterogeneously on dislocations.

The slow age hardening response of the Al-2.5 Cu alloy, the insufficient quantity of the Al-5Cu alloy, and also because it had been noticed that the large grain size in the binary alloys prevented repeatable and representative measurements of tensile data, made it necessary to request additional material with a minimum of 4% Cu from Reynolds. This alloy, which contains additions of 0.1% Zr for grain growth control and was processed to produce a strong cube recrystallization texture after annealing, arrived at UVA shortly after the end of the reporting period. It has been aged for 168 hours @ 175°C with and without a tensile stress of 50 MPa and tensile specimens are currently being machined.

Modeling of the effect of preferentially aligned Θ'-precipitates on the yield stress anisotropy in textured material requires accurate quantitative data for the distribution of Θ' as a function of aging stress, temperature and grain orientation for all habit plane variants. Preparation of one TEM foil only allows measurements of number density and dimensions of Θ' for two of the three different {100} planes because only two planes can be tilted in an orientation perpendicular to the electron beam. Obtaining data for the third habit plane requires the preparation of a second TEM foil with a different orientation but containing the same grain. As a consequence, very large grained material is necessary. Tensile bars were prepared from an Al-4Cu casting without the addition of Zr. Repeated annealing, quenching and straining to 0.5% plastic deformation resulted in grains with diameters of up to 1 inch. The stress aging parameters were the same as above.

These measurements of the three dimensional precipitate distribution made it also necessary to refine the method that had been used to determine the angle between the load axis and each of the two habit planes on a TEM-image. Earlier measurements were found to be sometimes erroneous, because they had not accounted for image rotations due to tilting of the foil in the TEM. The new procedure utilizes the known orientation of the TEM foil in the specimen, the marked orientation of the aging stress on the TEM foil and the tilting angles in X- and Y-direction for an image with a (100) zone axis. It allows the calculation of the angle components between the stress

axis and the precipitates in the image plane and perpendicular to it.

Although the measurements have not yet been completed, the results appear reasonably consistent with the following equation for the distribution of Θ', which predicts the influence of a tensile aging stress on the relative volume fraction of precipitates on each variant of {100} for all grain orientations:

$$V_{f(100)} = \sum V_{fi} \frac{\sin\varphi_{(100)}}{\sin\varphi_{(100)} + \sin\varphi_{(010)} + \sin\varphi_{(001)}} \qquad [3]$$

with V_{fi} = Volume fraction of Θ' on each {100} plane, and φ_i = Angle between the normal of each habit plane and the tensile stress axis.

Hosford's plastic inclusion model, as well as the model developed by Bate were modified to account for the effects of non-random precipitate distributions on yield stress anisotropy. In the calculation of N and $||\gamma||$, in Equations [1] and [2], the actual volume fractions on each variant of the habit plane were introduced, instead of assuming identical volume fractions on all variants. In the plastic inclusion model, N_{avg} was replaced by:

$$N_{aligned} = 1/ V_f \, (V_{f\,(100)} N_{\,(100)} + V_{f\,(010)} N_{\,(010)} + V_{f\,(001)} N_{\,(001)}) \qquad [4]$$

$||\gamma||_{aligned}$ was calculated accordingly. Using Mark Lyttle's program and using Equation [3] for the calculation of $V_{f(I)}$, the yield stress anisotropy caused by a uniaxial tensile stress can be calculated for all textures. Fig. 4 represents results of the calculations for a single grain in a {100} [100] orientation. This configuration can be viewed as the upper limit for anticipated anisotropy effects due to preferential precipitation of Θ' under the influence of a tensile aging stress. It is representative of a material with an ideally strong cube texture and with two {100}-planes parallel to the load axis, each of them containing 50% of the total volume fraction of Θ'.

Resulting curves for N and $||\gamma||$ are compared in Fig. 4a and 4b with the curves for a grain with identical orientations but conventionally aged, i.e. aged without stress. The curves of N_{random} and $||\gamma||_{random}$ exhibit a minimum under 45°, indicating that at this angle the Θ' precipitates contribute the least to the yield strength of the material . Selective precipitation results in an

increase in the strengthening factor N at 45° from about 0.66 to 0.75. The different distribution should not have any influence on yield stress parallel and perpendicular to the rolling direction. The elastic inclusion model predicts an almost negligible effect for all test directions (Fig. 4b).

The predicted influence on the yield stress is demonstrated in Fig. 4c for the plastic inclusion model. Stresses are normalized by the yield strength in the rolling direction to enable a comparison between the different aging conditions. Single phase FCC material , represented by the matrix curve, exhibits its highest yield strength under 45 degrees, because the Taylor factor is highest in this orientation. Because the strengthening factor of Θ' precipitates follows an opposite trend, conventionally aged material exhibits a much less pronounced anisotropy. The modified plastic inclusion model predicts an increase in anisotropy of about 10% for stress aged material. In more complex textured material the predicted influence of a tensile aging stress is even smaller. However, the applicability of either model still needs to be experimentally verified.

Conclusions

In combination with a random crystallographic texture Al-Cu-Mg-Ag alloy, application of a tensile stress during aging resulted in minor changes in yield anisotropy. The experiments showed that a critical aging temperature, i.e. approximately 190°C for Θ' must not be exceeded to achieve stress induced preferential precipitation. After aging with an externally applied tensile stress the relative number density of Θ' precipitates on each {100} habit plane variant was approximately proportional to the stress component acting parallel to them.

A theoretical analysis based on the plastic inclusion model (Hosford) and on the elastic inclusion model (Bate) predict even for strongly textured material only minor influences of aligned Θ' on anisotropy after tensile stress aging. However, more pronounced effects are anticipated for different aging stress configurations and also for the effects of stress induced alignment of Ω.

Tasks for the next reporting period

As of December 31, 1996, this project is no longer included in the NASA-UVA LA^{2}ST program.

References

1. G.I. Taylor, "Plastic Strain in Metals," J. Inst. Metals 62, p. 307 (1938).

2. J.F.W. Bishop and R. Hill, "A Theory of the Plastic Distortion of a Polycrystalline Aggregate Under Combined Stresses," Phil. Mag. 42, p. 414 (1951).

3. W.F. Hosford and R.H. Zeisloft, " The Theory of Age-Hardened Al-4 Pct Cu Single Crystals During Plane-Strain Compression," Met Trans. 3, p. 113-121 (1972).

4. P. Bate, W.T. Roberts and D.V. Wilson, "The Plastic Anisotropy of Two-Phase Aluminum Alloys—I. Anisotropy in Unidirectional Deformation," Acta Metall 29, p. 1797-1814 (1981).

5. B. Skrotzki, G.J. Shiflet, E.A. Starke, Jr., "On the Effect of Stress on Nucleation and Growth of Precipitates in an Al-Cu-Mg-Ag Alloy," Metall Trans. A, 27A, p. 3431-3444 (1996).

6. M.T. Lyttle and J.A. Wert, " The Plastic Anisotropy of an Al-Li-Cu-Zr Alloy Extrusion in Unidirectional Deformation," Metall. Trans. A, 27A, p. 3503-3511 (1996).

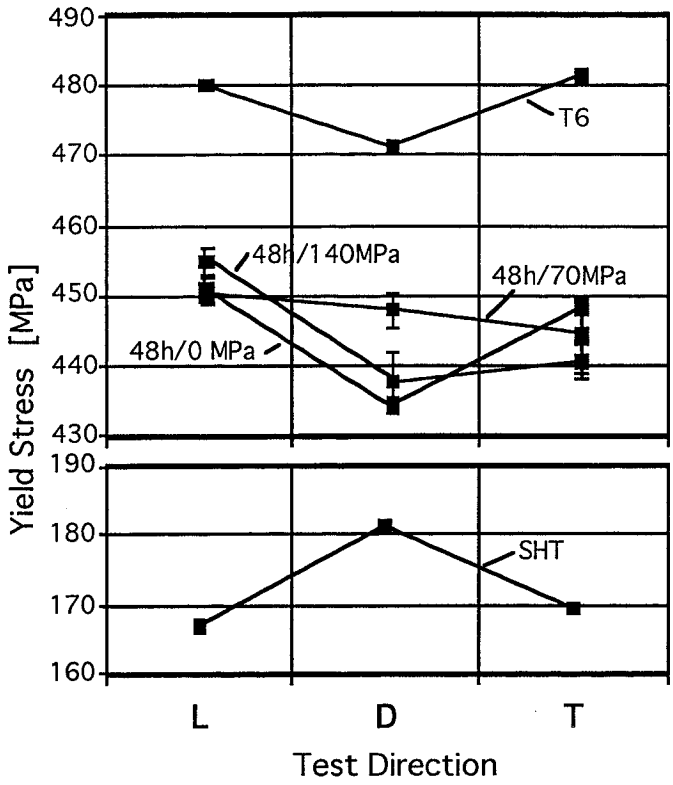

Fig.1 Influence of tensile aging stress on yield stress anisotopy in modified Al2519. Aging stress was parallel to L-direction.

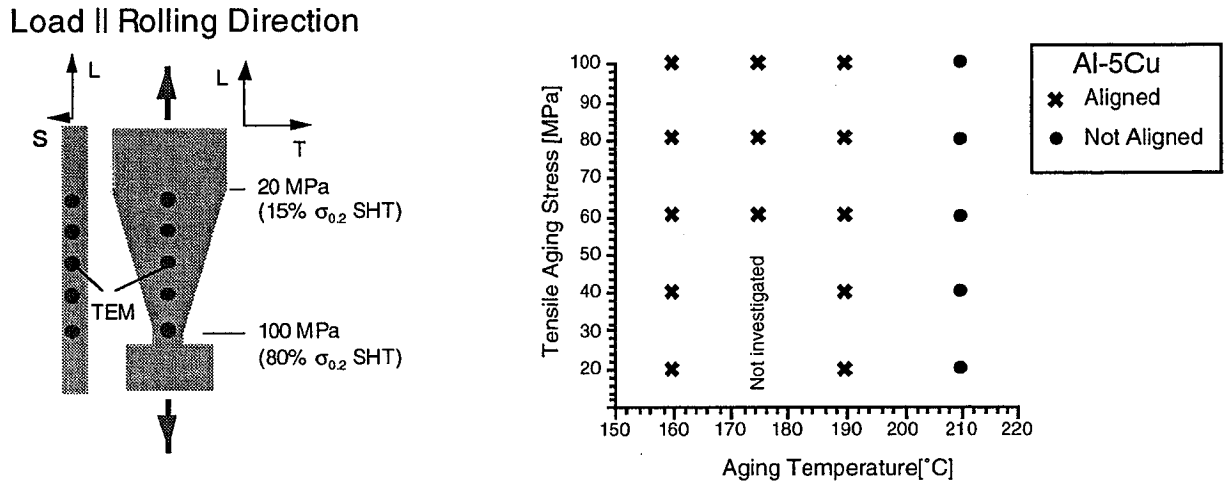

2a, Specimen layout 2b, Results

Fig. 2 Influence of combinations of aging temperature and stress on aligned precipitation of θ' in Al-5Cu.

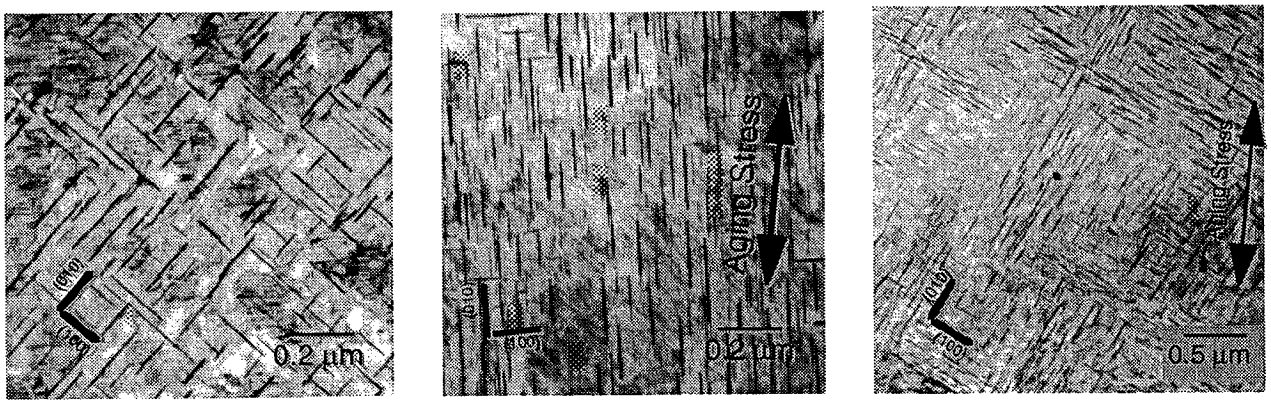

a, b, c,

Fig. 3 Influence of tensile aging stress on distribution of q' in Al-5Cu. TEM, Brightfield, (100) zone axis. a, :No aging stress; Random b,: Stress aging below critical temperature: Aligned. c,: Stress aging above critical temperature: Bands

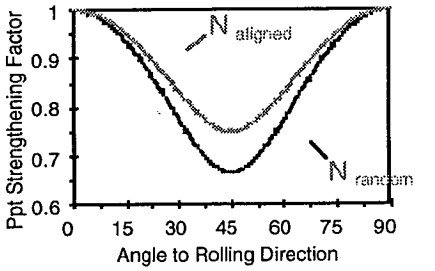

a, Precipitate Strengthening Factor

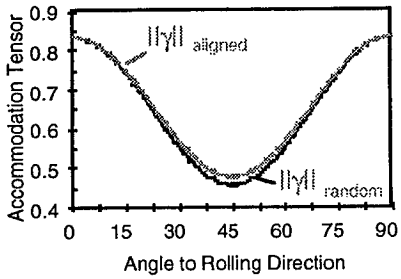

b, Accomodation Tensor

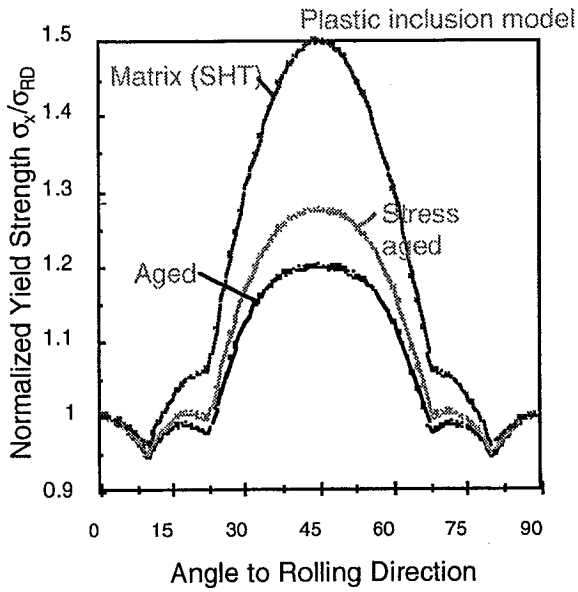

c, Normalized Yield Strength

Fig. 4 Predicted anisotropy effects due to precipitation of θ' for strong cube texture. Comparison of conventional aging (random) with stress aging in tension (aligned).

Project 4: Creep Behavior and Microstructural Stability of Al-Cu-Mg-Ag and Al-Cu-Li-Mg-Ag Alloys

Susan M. Kazanjian, Ning Wang and Edgar A. Starke, Jr.

Research Objectives

To assist in the development of a high speed civil aircraft by NASA and airframe manufacturers, the University of Virginia (UVA) has been examining the creep behavior of several candidate aluminum alloys. Creep strains of alloys C415, C416 and ML377 under stresses and temperatures predicted to be experienced when cruising at Mach 2.0, will be measured and compared to those alloy 2618 (CM.001) which is currently in use on the supersonic Concorde. Microstructural evolution in the vicinity of the grain boundaries of these alloys will be examined directly in the transmission electron microscope and by fracturing crept specimens at cryogenic temperatures to expose grain facets. Variation in number density and size of grain boundary precipitates as the severity of creep conditions increases will be related to creep behavior.

Background and Approach

The high speed civil transport (HSCT) is considered critical to the future competitiveness of the U.S. aircraft industry. Lightweight structural materials with long-term resistance to thermomechanical fatigue, creep and environmental degradation at operating temperatures are required to obtain the speed, payload and range necessary to make the aircraft economically feasible. Aluminum alloys are viable candidates for a major portion of a supersonic aircraft which does not exceed ultimate cruising speeds of Mach 2.0, since the skin temperature would remain below 100°C.[1] Consequently, NASA-Langley Research Center (LaRC), ALCOA, Allied-Signal, Boeing, McDonnell Douglas, Reynolds Metals and (UVA) have joined in a research effort to identify the most promising aluminum-based materials with respect to major structural use on the HSCT and to further develop those materials, and ii) assess the materials through detailed trade and evaluation studies with respect to their structural efficiency on the HSCT.[2] The focus of the current task is to investigate creep behavior of the most promising alloys under conditions likely to be imposed by Mach 2.0 service.

Initial investigation into candidate alloy classes concluded that age-hardenable 2XXX

alloys, with and without lithium, possessed attractive mechanical properties and thermal stability to replace 2618 for supersonic aircraft application. Alloy 2618 (CM.001) is an Al-Cu-Mg alloy with added Fe and Si to form intermetallics. The variant currently in use on the Concorde, CM.001, is produced under a proprietary thermo-mechanical processing schedule designed to meet the creep goals of the Concorde design while achieving the requirements for durability, fracture toughness and strength. The three HSCT candidate alloys were developed to provide substantial improvement in toughness and strength while continuing to meet the creep goal. Table I identifies the room temperature (RT) yield strengths and compositions of each of the alloys under test, comparing them to 2618.[3]

Table I: Alloys Under Test

Alloy	**RT Yield Strength**	**Composition (wt %)**									
	MPa	**Al**	**Cu**	**Li**	**Mg**	**Mn**	**Ag**	**Zr**	**Fe**	**Si**	**Ni**
2618 (CM.001)	386	Bal	2.5	-	1.5	-	-	-	1.1	0.22	1.1
ML377-T8	517	Bal	3.5	1.0	0.4		0.4	0.13		-	-
C415-T8	490-517	Bal	5.00	-	0.80	0.60	0.50	0.13	0.06	0.04	-
C416-T8	483-496	Bal	5.40	-	0.50	0.30	0.50	0.13	0.06	0.04	-

Alloys C415 and C416 are modifications of alloy 2519 which was found to have higher thermal stability than 2618. Compared to 2618, they possess lower volume fractions of constituents and incoherent dispersoids which have an adverse effect on fracture toughness. A strength advantage of about 10% over 2519, realized with additions of Ag and Mg, is attributable to the replacement of the Θ‘ phase which precipitates on {100} planes with Ω which precipitates on {111} planes.[4] The alloys contain less Cu than 2519, and sufficient Ag and Mg to promote Ω phase formation. Both also contain Mn in the form of submicron $Al_{20}Cu_2Mn_3$ particles and Zr in an unidentified form for grain structure control. In the T8 temper condition with 2% stretch

prior to aging, C415 possesses higher ambient and elevated temperature strength, while C416 appears to be more thermally stable and creep resistant.[3]

Of the two lithium bearing alloys originally considered HSCT candidates, ML377 is now preferred over RX818. Both alloys possess good strength and elongation combinations. However, while RX818 exhibits higher ambient temperature strength, after 3000 hours exposure to service temperatures, this alloy loses up to 30% of its original strength and fracture toughness. ML377 was developed as a recrystallized version of RX818. After thermal exposure, ML377 exhibited superior fracture toughness with little sacrifice of strength.[5] The anisotropy of rolled sheet is also significantly reduced from that of the unrecrystallized RX818.[5]

NASA's current effort is to identify a stress level for each material below which the design goal of less than 0.1 percent creep strain over the 60,000 hour lifetime of the aircraft can be met.[6] Consequently, testing at UVA is being conducted at temperatures of 107°C and 135°C under stresses of 138, 172 and 207 MPa. These low stresses and temperatures result in the majority of the tests never reaching secondary stage creep. This is appropriate from a design standpoint since most of the life of the alloy in service would be spent in the primary creep regime. Unfortunately, fundamental analysis of creep mechanisms within primary creep is difficult due to the complexity of microstructural changes usually occurring.

Strain gaged flat tensile specimens were provided by NASA LaRC for creep testing in accordance with ASTM Specification No. E139. Strain over time was recorded from the output of two strain gages per specimen, then averaged to display curves. Duration of creep exposure was dictated by NASA LaRC personnel in consultation with Lockheed.

Miniature notched impact specimens were machined from one half of the gage length of the tested specimens. These were cooled in liquid nitrogen and fractured under impact to promote intergranular fracture, thus exposing grain facets. Fracture surfaces were examined in the scanning electron microscope (SEM) to determine the effect of creep conditions upon the grain boundary environment. This method provides a sensitive test of any alteration that may be occurring at the grain boundaries, while allowing sufficient remaining material to be analyzed by transmission electron microscopy (TEM). Both of these factors present advantages over post-creep tensile testing which destroys any deformation structure developed during creep when ductile elongation occurs and must be performed with an entire creep specimen to provide sufficient gripping surface, leaving no as-crept material for microstructural evaluation.

Post-test microstructures were examined in the TEM. Foils were prepared by twin-jet electropolishing in a solution of 1 part nitric acid to 3 parts methanol at -30°C.

Progress During the Reporting Period

Creep curves for C415, C416 and CM.001 tested at 107°C (225°F) are shown in Figure 1. Curves generated at 135°C (275°F) are given in Figure 2. These curves do not include initial instantaneous elastic straining of the specimens. Specimens of C415 and 2618 are continuing under test at 107°C and 207 MPa, conditions of particular interest to NASA.

Because of the strength advantages C415 and C416 posses over CM.001, applied test stresses are considerably more severe for the CM.001 alloy, resulting in larger absolute creep strains. However, a direct comparison of creep performance is certainly valid when considering test parameters which reflect the operating conditions of the aircraft. In this regard, C415 (and, therefore, C416) outperforms CM.001 at equivalent test conditions of 107°C and 207 MPa. ML377 exceeds the performance of C415 in direct comparison at 135°C and 172 MPa. Thus, all of the candidate alloys have improved creep performance over CM.001 along with the strength and fracture toughness advantages they offer.

Post-test SEM examination of impact fractured specimens revealed appreciable increases in microvoid size and density on grain facets as well as rising percentage of intergranular fracture in the C415 material for creep conditions of increasing severity, as apparent in Figure 3. Under the conditions tested to date at UVA, ML377 and C416 do not exhibit these obvious microstructural changes. This may be a controlling factor in the reduction of creep strain for C416 and ML377.

TEM examination of the grain boundary area of C415 before and after creep confirms that the increase in size and density of microvoids in the SEM images corresponds to increasing size and number density of precipitates along the boundaries. This is evident in Figure 4 which presents images of grain boundary area both before and after creep of C415. In these views, the boundary is tilted with respect to the electron beam to show the number density and size of precipitates within the boundary through the thickness of the foil. Electron dispersive spectroscopy (EDS) and electron diffraction patterns indicate that these grain boundaries are either S' or Ω or both.

The increase in slope of the creep curve of C415 over ML377 at 135°C, 172 MPa may be

a consequence of changes in precipitate morphology at the grain boundary which occur in C415, but not in ML377 under these conditions. Further research on ML377 and C416 and investigation of the microstructure of crept CM.001 material will help explore this hypothesis.

Conclusions

The creep behavior of three candidate alloys was examined and compared to the alloy in current use on the Concorde to identify the most promising aluminum-based materials for major structural use on the HSCT. The microstructural evolution in the vicinity of the grain boundaries received particular attention. Results indicate that the candidate alloys have much superior creep resistance than the Concorde alloy. Creep induced change in precipitates at the grain boundaries was observed in the alloy which exhibits the highest creep strain of the three candidate alloys. The other two alloys developed no detectable microstructural changes at grain boundaries under the creep conditions tested.

Tasks for the Next Reporting Period

Creep tests on C415 and CM.001 materials are continuing under conditions of the most interest to NASA, 107°C and 207 MPa. Testing will continue through the primary creep regime until secondary creep is achieved. CM.001 will be also tested under a lower stress condition, 138 MPa, that is deemed more fair to its original design strength and under conditions that will allow direct comparison to the other candidate alloys.

The two alloys exhibiting the highest creep resistance, C416 and ML377, will be exposed to higher stress and temperature creep conditions.

Specimens tested under additional creep conditions have been requested from NASA for cryogenic fracture and SEM and TEM examination.

Material exposed to temperatures equivalent to those of the creep tests above, but not subjected to stress at temperature have also been requested from NASA in order to compare microstructures under TEM examination.

References

1. Harpur, N.F., "Concorde Structural Development," *J. Aircraft,* v.5, no. 2, 176-183 (April 1968).

2. NASA Grant No. NAG 1-745, "Aluminum-Based Materials for High Speed Aircraft."

3. Karabin, L., *NASA-UVA Light Aerospace Alloy and Structure Technology Program - Supplement: Aluminum Based Materials for High Speed Aircraft*, Final Report Grant No. NAG 1-745, University of Virginia, SEAS Report No. UVA/528266/MSE96/120, 1-30, (May 1996).

4. Starke, E.A., *Jr., NASA-UVA Light Aerospace Alloy and Structure Technology Program - Supplement: Aluminum Based Materials for High Speed Aircraft*, NASA Conference Report 4517, 1993.

5. Cho, A., Greene, R.E., Skillingberg, M.H. and Fielding, P.S., "Al-Li Alloy Development at Reynolds Metals Company for Aerospace Applications," *Aluminum-Lithium Alloys for Aerospace Applications Workshop- NASA Conference Publication 3287,* ed. B.H. Bhat, T.T. Bayles and E.J. Vesely, Jr., 17-25 (1994).

6. *Accelerated Aging of Materials and Structures,* National Materials Advisory Board, Commission on Engineering and Technical Systems, National Research Council, NMAB-479, National Academy Press, Washington, D.C. 1996.

7. Skrotski, B., Hargarter, H. and Starke, E.A., Jr., "Microstructural Stability under Creep Conditions of two Al-Cu-Mg-Ag," *Materials Science Forum: Aluminum Alloys - Their Physical and Mechanical Properties*, Proceedings ICAA5, ed. J.H. Driver, B. Dubost, F. Durand, R. Fougeres, P. Guyot, P. Sainfort and M. Suery, Transtec Publications, Switzerland, v. 217-222, 1245-1250, (1996).

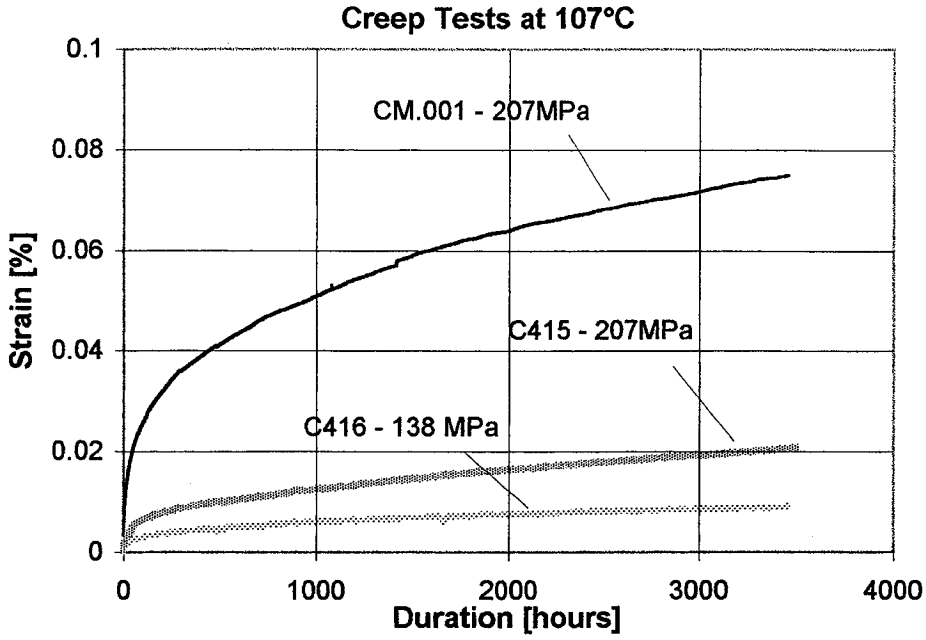

Figure 1. Creep curves acquired at 107°C.

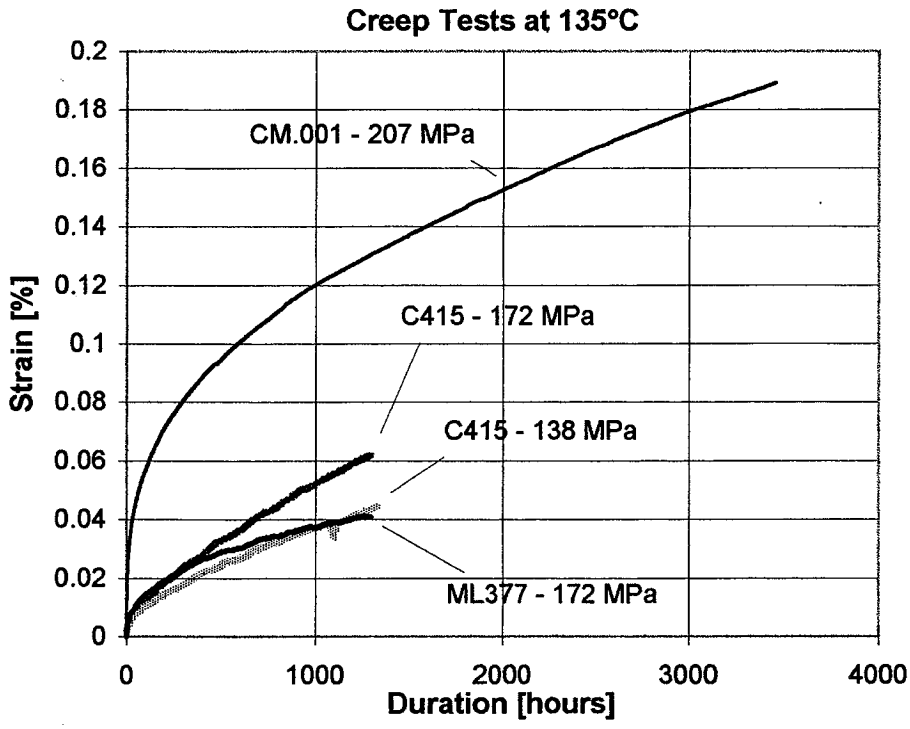

Figure 2. Creep curves acquired at 135°C.

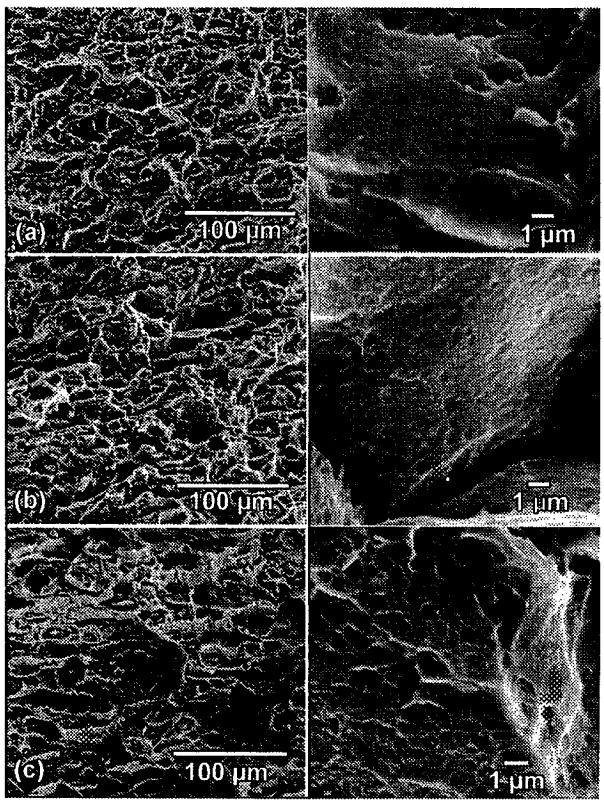

Figure 3. Figure 3. SEM fractographs of C415 (a) prior to creep, (b) exposed to 135°C, 138 MPa for 1300 hours and (c) exposed to 135°C, 172 MPa for 1300 hours. Increasing severity of creep conditions is accompanied by a higher percentage of intergranular fracture and by a higher density of voids on the exposed grain facets.

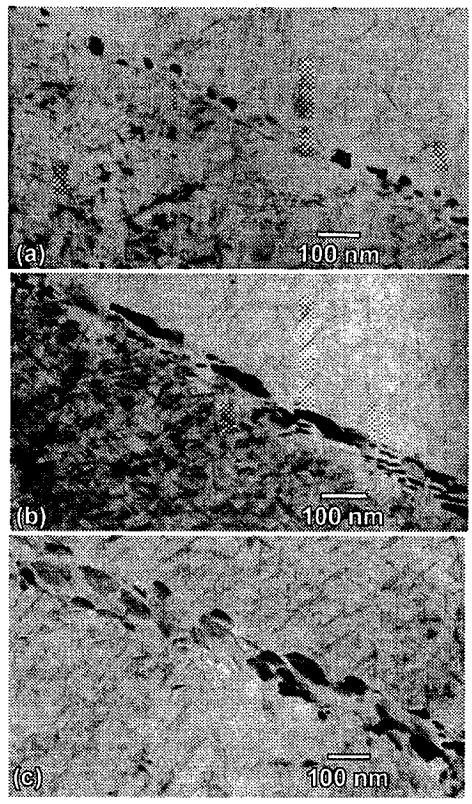

Figure 4. TEM micrograph of C415 (a) prior to creep, (b) exposed to 135°C, 138 MPa for 1300 hours and (c) exposed to 135°C, 172 MPa for 1300 hours. Precipitates within the grain boundary region increase in size and number as severity of creep exposure increases.

DISTRIBUTION LIST

1-4	Mr. D.L. Dicus Contract Monitor Metallic Materials Branch, MS 188A NASA Langley Research Center Hampton, VA 23681-0001
5-6*	NASA Scientific and Technical Information Facility P.O. Box 8757 Baltimore/Washington International Airport Baltimore, MD 21240
7	Mr. Joseph S. Murray Grants Officer, M/S 126 NASA Langley Research Center Hampton, VA 23681-0001
8	Dr. Mark J. Shuart Materials Division, MS 188M NASA Langley Research Center Hampton, VA 23681-0001
9	Dr. Charles E. Harris Materials Division, MS 188M NASA Langley Research Center Hampton, VA 23681-0001
10	Mr. W. Barry Lisagor Metallic Materials Branch, MS 188A NASA Langley Research Center Hampton, VA 23681-0001
11	Dr. Robert S. Piascik Mechanics of Materials Branch NASA Langley Research Center Hampton, VA 23681-0001
12	Mr. W.D. Brewer Metallic Materials Branch, MS 188A NASA Langley Research Center Hampton, VA 23681-0001

13 Mr. Thomas T. Bales
Metallic Materials Branch, MS 188A
NASA Langley Research Center
Hampton, VA 23681-0001

14 Ms. Marcia S. Domack
Metallic Materials Branch, MS 188A
NASA Langley Research Center
Hampton, VA 23681-0001

15 Dr. Stephen J. Hales
Metallic Materials Branch, MS 188A
NASA Langley Research Center
Hampton, VA 23681-0001

16 Mr. R. Keith Bird
Metallic Materials Branch, MS 188A
NASA Langley Research Center
Hampton, VA 23681-0001

17 Mr. Eric K, Hoffman
Metallic Materials Branch, MS 188A
NASA Langley Research Center
Hampton, VA 23681-0001

18 Ms. Terryl A. Wallace
Metallic Materials Branch, MS 188A
NASA Langley Research Center
Hampton, VA 23681-0001

19 Ms. Joan G. Funk
HSR Project Office, MS 119
NASA Langley Research Center
Hampton, VA 23681-0001

20 Mr. Rodney H. Ricketts
HSR Project Office, MS 119
NASA Langley Research Center
Hampton, VA 23681-0001

21 Mr. Edward P. Phillips
Mechanics of Materials Branch, MS 188E
NASA Langley Research Center
Hampton, VA 23681-0001

22 Dr. Alex Cho
Reynolds Metals Co.
4th and Canal Street
Richmond, VA 23261

23 Mr. E.A. Colvin
Alcoa Technical Center
Route 780, 7th Street Road
Alcoa Center, PA 15069

24 Dr. L.M. Karabin
Alcoa Technical Center
Route 780, 7th Street Road
Alcoa Center, PA 15069

25 Dr. Ravi Kahandal
McDonnell Douglas Aerospace
Mail Stop 36-90
3855 Lakewood Boulevard
Long Beach, CA 90846

26 Dr. William E. Quist
Boeing Commercial Airplane Group
MS 6H-CJ
P.O. Box 3707
Seattle, WA 98124-2207

27 Dr. John Papazian
Northrop Grumman Corporation
ATDC, A01-26
Bethpage, NY 11714-3581

28 Dr. Richard Lederich
McDonnell Douglas Aircraft Company
Mail Stop 111-1041
P.O. Box 516
St. Louis, MO 36166

29 Mr. David J. Chellman
Lockheed Martin Aeronautical Systems
Dept. 73-C1, Zone 0648
86 South Cobb Drive
Marietta, GA 30063-0648

30 Dr. Malcolm Ozelton
Manager, Metallic & Ceramic Materials
Northrop Corporation, B-2 Division
8900 E. Washington Boulevard
T241/GK
Pico Rivera, CA 90660-3737

31 Dr. James Staley
Alcoa Laboratories
Alcoa Technical Center
Route 780, 7th Street Road
Alcoa Center, PA 15069

32 Mr. Rodney R. Boyer
Boeing Commercial Airplane Group
MS 6H-CJ
P.O. Box 3707
Seattle, WA 98124-2207

33 Dr. Govind Chanani
Northrop Grumman Corporation
One Hornet Way, MC 9B70/W8
El Segundo, CA 90245

34 Dr. Michael T. Hahn
Northrop Grumman Corporation
T241/GK
8900 E. Washington Boulevard
Pico Rivera, CA 90660-3737

35 Professor Henry J. Rack
Clemson University
School of Materials, Chemical & Engineering
208 Rhode Hall
Clemson, SC 29634-0921

36 Dr. Pat Martin
Rockwell Science Center
1049 Camino Dos Rios
Thousand Oaks, CA 91360

37 Mr. John Fanning
TIMET
P.O. Box 2128
Henderson, NV 89009

38	Mr. J.R. Wood RMI Titanium Company 1000 Warren Avenue Niles, OH 44446
39-40	E.A. Starke, Jr.; MS&E
41-42	R.P. Gangloff; MS&E
43	G.E. Stoner; MS&E
44	J.A. Wert; MS&E
45	J.R. Scully; MS&E
46	R.G. Kelly; MS&E
47	M. Rodeffer, Clark Hall
48	SEAS Preaward Research Administration
**	SEAS Postaward Research Administration

* One reproducible copy
** cover letter

Updated: April, 1997